The optical volume scattering function in a surf zone inverted to derive sediment and bubble particle subpopulations

Michael Twardowski,[1] Xiaodong Zhang,[2] Svein Vagle,[3] James Sullivan,[1] Scott Freeman,[1] Helen Czerski,[4] Yu You,[5] Lei Bi,[5] and George Kattawar[5]

Received 31 May 2011; revised 21 December 2011; accepted 23 December 2011; published 21 February 2012.

[1] The effects of particle fields including bubbles on the optical volume scattering function (VSF) were investigated in the surf zone off Scripps Pier as part of an ongoing effort to better understand the underlying dynamics in the VSF in the subsurface ocean. VSFs were measured at 20 Hz at angles spanning 10°–170° in 10° increments with a device called the Multiangle Scattering Optical Tool (MASCOT). Modification of the phase function was observed in passing suspended sediment plumes, wave-injected bubble plumes, and combinations of these particle populations relative to the background. Phase function enhancement in the 60°–80° range was observed in association with bubble plumes, consistent with theoretical predictions. VSFs were inverted to infer size distributions and composition using a least squares minimization fitting procedure applied to a library of phase functions, each representing a lognormally distributed subpopulation with refractive index and coating, where applicable. Phase functions representative of nonspherical mineral particle subpopulations were computed using discrete dipole approximation (DDA) and improved geometric optics method (IGOM) techniques for randomly oriented, asymmetric hexahedra. Phase functions for coated bubbles were computed with the Lorenz-Mie theory. Inversion results exhibited stable solutions that qualitatively agreed with concurrent acoustical measurements of bubbles, aggregate particle size distribution expectations, and anecdotal videography evidence from the field. Although a comparable inversion with a library that assumed spherical shaped particles alone provided less stable results with some incorrectly assigned subpopulations, several dominant subpopulation trends were consistent with the results obtained using nonspherical representations of mineral particles.

Citation: Twardowski, M., X. Zhang, S. Vagle, J. Sullivan, S. Freeman, H. Czerski, Y. You, L. Bi, and G. Kattawar (2012), The optical volume scattering function in a surf zone inverted to derive sediment and bubble particle subpopulations, *J. Geophys. Res.*, *117*, C00H17, doi:10.1029/2011JC007347.

1. Introduction

[2] Time- and space-dependent radiance distributions through surface waters are a function of the shape of the incident distribution on the surface, modification by the sea surface itself from wavy topography and transmission characteristics, and alteration by the inherent optical properties (IOPs) of the subsurface ocean (the ongoing special section "Recent Advances in the Study of Optical Variability in the Near-Surface and Upper Ocean" in *Journal of Geophysical Research*). Knowing the IOPs and their subsurface dynamics, radiance distributions can be computed from incident light fields using the equation of radiative transfer, now embedded with plane-parallel constraints in commercially available code (e.g., Hydrolight, Sequoia Inc.) [*Mobley et al.*, 1993] or in full 3-D embodiments with vector polarization [*You et al.*, 2011a]. Disregarding inelastic effects such as Raman scatter and fluorescence, the IOPs required to compute radiance fields are the volume scattering function (VSF) and absorption coefficient. Absorption only changes intensity, not directional properties of individual waves. Thus, once in the subsurface ocean, the VSF is the dominant parameter affecting the dynamics of radiance field distributions. VSF dynamics in turn are controlled by particle fields including bubbles, with scattering by pure seawater being a stable component [*Zhang et al.*, 2009, 2011].

[3] Working toward the goal of better understanding the dynamics of subsurface VSFs, the particle fields responsible, and the impacts on radiance fields and image transmission, this study focuses on measuring the high-frequency dynamics of the VSF with subsequent inversion to solve for

[1]Department of Research, WET Labs, Narragansett, Rhode Island, USA.
[2]Department of Earth System Science and Policy, University of North Dakota, Grand Forks, North Dakota, USA.
[3]Institute of Ocean Sciences, Fisheries and Oceans Canada, Sidney, British Columbia, Canada.
[4]Graduate School of Oceanography, University of Rhode Island, Narragansett, Rhode Island, USA.
[5]Department of Physics and Astronomy, Texas A&M University, College Station, Texas, USA.

0148-0227/12/2011JC007347

size distributions and composition of particle subpopulations in the surf zone at Scripps Pier, California. With respect to developing and testing the inversion technique, the surf zone had several clear benefits as a study site, as (1) the particle population was chiefly composed of two, well-defined types, suspended quartz-dominated mineral sand (identified by scanning electron microscopy and energy dispersive spectroscopy on collected samples) and injected bubbles from wave breaking; (2) local sediment plume advection or bubble injection could be directly confirmed visually; (3) scattering from bubbles can be readily modeled from theory; (4) background water clarity was excellent, optimizing the measurement dynamic range; and (5) the pier enabled easy access and a stable platform. Particle composition is expected to be highly dynamic in space and time in the surf zone and subsurface waters in general due to proximal phenomena such as breaking waves, resuspension (if shallow), advection, the coating of bubbles from microlayer organic films, and selective accumulation of buoyant particles from the water column.

[4] The link between particle fields and VSFs in the ocean is currently not well understood. This is a consequence of a historical dearth of suitable models to describe scattering by complex (i.e., intricate shape, heterogeneous composition) particles, the inherent complexity of having a wide diversity of particle types in every drop of seawater, and the lack of availability of instrumentation able to provide the necessary data for model initialization and validation (and model development, when some empiricism is involved). Most models describing scattering by complex particles have made the first-order approximation that a population of complex particles may be represented by an equivalent population of homogeneous spherical particles [*Gordon and Brown*, 1972; *Zaneveld and Pak*, 1973; *Brown and Gordon*, 1973; *Zaneveld et al.*, 1974; *Jonasz and Prandke*, 1986; *Ulloa et al.*, 1994; *Twardowski et al.*, 2001; *Zhang et al.*, 2002, 2011]. This is the well-known Lorenz-Mie theory scattering. The degree to which Lorenz-Mie theory can be used to represent scattering by a complex particle population is arguable, although it should be recognized that certain aspects of scattering are nearly immune to shape and internal structure dependencies while other aspects exhibit strong dependencies [*Zhang et al.*, 2011]. For example, the diffraction pattern in the near-forward direction is almost entirely dependent on particle cross-sectional area, with internal refractive index structure having a small influence [*Agrawal and Pottsmith*, 2000]. This is the principle underlying diffractometry-based particle sizing techniques. Also, refractive index and shape play a small role in determining the shape of visible light scattering distributions for particles less than about 1–2 μm in size. The largest uncertainties with the homogeneous spherical assumption are for larger particles in the backward direction [*Zhang et al.*, 2011]. The most obvious anomalies with this theory are local maxima typically observed in the 90°–120° region, especially for particles with high refractive index. These are spherical lensing effects that are not observed in VSFs of complex nonspherical particles or oceanic populations [*Sullivan and Twardowski*, 2009]. Computations of scattering have also been carried out for simple, nonspherically shaped particles such as ellipsoids and cylinders [e.g., *Mishchenko et al.*, 2000; *Clavano et al.*, 2007] and for more complex particles for unique, specific cases [*Gordon*, 2007], although when considering the complexity of particles in the ocean, there is no clear evidence that assuming simple nonspherical shapes is better than assuming sphericity in modeling the scattering characteristics of an all-inclusive assemblage of natural oceanic particles.

[5] Inversion models typically aim to derive particle characteristics from optical measurements based on deductions from carrying out multiple iterations of the forward problem described above. The basic premise is that particles of different sizes, composition, and shape will scatter light as a function of angle in different relative amounts. For example, optically "hard" particles with high refractive index such as minerals, scatter or reflect light more intensely in the backward direction than "soft" particles such as water-filled biological cells [*Twardowski et al.*, 2001]. It is obvious that the accuracy of any inversion model can only be as good as the accuracy and the required assumptions associated with the forward model and any embedded empiricism. Previous optical inversion efforts to discriminate particle composition have generally only been able to solve for the bulk (or "averaged") refractive index of the population, which is a close analog for bulk particle density [*Gordon and Brown*, 1972; *Zaneveld and Pak*, 1973; *Carder et al.*, 1974; *Twardowski et al.*, 2001], although some inversions have solved for multiple subpopulation components [*Brown and Gordon*, 1973; *Zaneveld et al.*, 1974; *Kopelevich*, 1983; *Jonasz and Prandke*, 1986].

[6] Inversion of light scattering by a collection of natural particles to obtain the size and composition details of all the particles is clearly not possible as the number of particle population parameters will always grossly exceed the number of unique measured scattering parameters. We have recently demonstrated, however, that inversions may be developed that are able to solve for size distributions and refractive indices for several particle subpopulations if the number of population parameters is kept small and if they are carefully chosen [*Zhang et al.*, 2011].

[7] In this work, scattering theory and the principle of the inversion technique are presented first. Scattering functions for asymmetric hexahedra particles computed from the discrete dipole approximation (DDA) and the improved geometrics optics method (IGOM) are used to approximate scattering from suspended minerals. This is followed by a detailed description of a VSF device that was custom built to collect the required measurements. The device resolves the VSF from 10° to 170° at 20 Hz, fast enough to resolve the high-frequency dynamics observed in subsurface waters. Bubble clouds alone show substantial evolution in size distributions over time periods less than 1 s [*Deane and Stokes*, 1999]. Finally, results of VSF measurements and inversion are presented, including a comparison of nonspherical and spherical assumptions in initializing the model, with concluding remarks.

2. Theory

[8] The VSF describes the angular dependence of scattered light from an incident unpolarized beam in units of $m^{-1}\ sr^{-1}$. It is defined as the radiant intensity $dI(\theta)$, scattered from a volume element dV, into a unit solid angle centered in direction θ, per unit irradiance E: $\beta(\theta) = (1/E)dI(\theta)/dV$. Assuming azimuthal symmetry and integrating the VSF over

all solid angles (i.e., 0 to π radians, or 0°–180°) yields the total scattering coefficient, b in units of m^{-1}. The phase function $\tilde{\beta}$ is the VSF normalized to total scattering, or $\beta(\theta) / b$ (sr^{-1}). Integrating the VSF in the backward direction (i.e., π/2 to π radians, or 90° to 180°) yields the backscattering coefficient, b_b in units of m^{-1}, which is of particular importance to remotely sensed water-leaving radiance. The backscattering ratio $\tilde{b}_b$, is defined as b_b / b. Subtracting the VSF contribution from pure seawater [*Zhang et al.*, 2009] allows derivation of the particulate fractions for the parameters above, namely $\beta_p(\theta)$, b_p, $\tilde{\beta}_p(\theta)$, b_{bp}, and $\tilde{b}_{bp}$. Particulate backscattering is typically no more than 1–2% of particulate scattering in natural waters [*Twardowski et al.*, 2001; *Sullivan et al.*, 2005]. A particulate scattering coefficient obtained by integrating the VSF only over the angular range measured by the Multiangle Scattering Optical Tool (MASCOT) device (see section 3.3) is represented as b_p^{10-170} and the associated backscattering ratio is $\tilde{b}_{bp}^{10-170}$.

[9] Bulk $\beta_p(\theta)$ measurements are a linear sum of the scattering from the individual particles as long as their concentration is not too high (typically must be separated by ~3 times the particle radii [*van de Hulst*, 1981]). Particles of different sizes and composition, represented optically as refractive index distribution and shape, scatter light differently, manifested in the angular distribution of the scattered light. Typically, smaller angles are more sensitive to particles of larger sizes (much greater than the wavelength of incident light), while larger angles are more sensitive to composition and smaller sizes. The decomposition of $\beta_p(\theta)$ into detailed information about the particle field can be described by

$$\beta(\theta) = \sum_{i=1}^{M} b_i(n(r), F(r), G(r), S(r))\tilde{\beta}_i(n(r), F(r), G(r), S(r), \theta), \quad (1)$$

where we have assumed that there are M particle subpopulations [*Zhang et al.*, 2011]. For each subpopulation, the phase function $\tilde{\beta}_i$ and b_i are determined by the distributions of particle refractive index $n(r)$, concentration $F(r)$, internal structure $G(r)$, and shape $S(r)$, each of which, in turn, is a function of particle radius r.

[10] Equation (1) can be rewritten in integral form, which is the classic Fredholm linear integral equation of the first kind with $\tilde{\beta}$ as the kernel function [*Twomey*, 1977]. To derive the optical and size properties of particles we need to invert equation (1) using the measured volume scattering function, $\beta_p(\theta)$. We have developed an inversion method retrieving the particle size distribution $F(r)$ and index distribution $n(r)$ from measured $\beta_p(\theta)$ [*Zhang et al.*, 2011]. The key to the inversion is to construct a library of subpopulation scattering functions (the kernel function) that is not only representative but also nonsingular. The method offers several advantages over earlier inversion techniques [*Brown and Gordon*, 1973; *Kullenberg*, 1974; *Zaneveld et al.*, 1974; *Schoonmaker et al.*, 1994; *Twardowski et al.*, 2001; *Zhang et al.*, 2002] in that (1) the lognormal size distributions employed offer a better representation of natural subpopulations than universal Junge-type (power law) distributions; (2) the kernel function is constructed to provide roughly balanced sampling in phase function space; and (3) the solution is derived from least squares minimization instead of trial and error.

3. Methods

[11] Field measurements of optical scattering were made with a prototype VSF sensor called the MASCOT, and an ac9 (WET Labs, Inc.) mounted in a custom cage with a 10 Hz SBE-49 conductivity-temperature-depth sensor (SeaBird Electronics, Inc.). Data from all instruments were concurrently multiplexed and time stamped with a WET Labs DH-4 into archives for later extraction, processing, and final merging. Deployment protocols followed that described by *Twardowski et al.* [1999] except where mentioned. Descriptions and protocols for calibration and processing for the scattering instruments are detailed below.

3.1. Deployment

[12] Data were collected off the south side of Scripps Pier, La Jolla, California, at piling 15, approximately 120 m from the entrance gate of the pier. This location was on the seaward edge of the surf zone region delineated by active wave breaking at the time. The pier is approximately 10 m above sea level. The sensor package was lowered to 0.5–1 m below mean sea level with a cable transmitting power and data. Data were visualized in real time on the pier. Video of surface water conditions and the sensor package was also recorded from the pier.

3.2. Absorption and Attenuation Measurements

[13] The ac9 measured the absorption a_{pg} and attenuation c_{pg} by dissolved and particulate material in water flowing through 25 cm path length cells at the rate of approximately 2 L min^{-1}. Plumbing intakes for absorption and attenuation were 20 cm from the MASCOT sample volume. The attenuation measurement is made with a 0.93° acceptance for scattered light. The absorption measurement uses a reflective tube with a diffuser in front of the detector [*Kirk*, 1992] to collect most of the scattered light in the cell, but there is a residual scattering error (about 10% of total scattering) that requires correction [*Zaneveld et al.*, 1994]. Scattering errors associated with the reflective tube absorption measurement were derived independently by convolving concurrently measured VSFs from the MASCOT with the scattering error weighting function W_a presented by *McKee et al.* [2008] for the ac9 reflective tube, i.e., $\int \beta(\theta) W_a(\theta) d\theta$.

[14] Field purified water blank calibrations were carried out within 2 days of in situ measurements. Blank measurements were made in the same orientation as deployment: horizontally with the ac9 secured in its cage. Corrections for time lags (the time required for a sample to travel from the plumbing intake to measurement inside the flow cell), the temperature and salinity dependence of pure water absorption and attenuation [*Pegau et al.*, 1997], drift, and absorption scattering error were applied in postprocessing. After all corrections, total particulate scattering b_p was then derived from $c_{pg} - a_{pg}$.

3.3. Volume Scattering Function Measurements

[15] Few measurements of oceanic VSFs in the 10° to 170° range have been made over the last several decades.

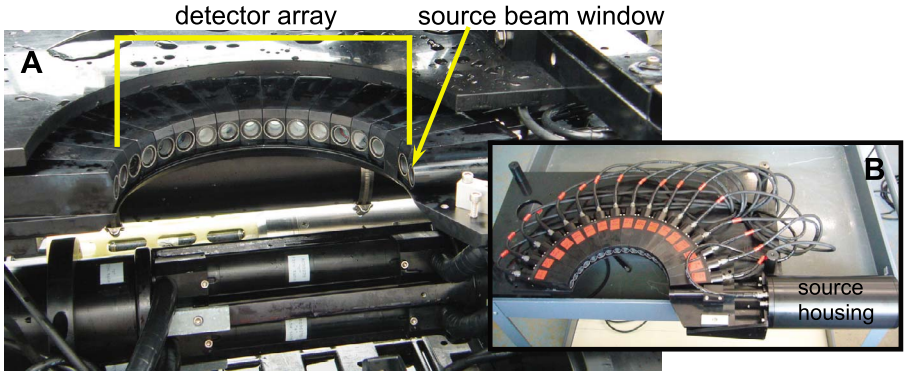

Figure 1. (a) Source and detector windows of MASCOT volume scattering function device mounted in deployment cage, and (b) MASCOT sensor in lab, showing source housing and semicircular detector array. The sample volume in the center of the semicircle averages about 1 cm^3.

Key obstacles have been (1) a single oceanic VSF typically has more than a 4 order of magnitude dynamic range in scattering intensity from near forward to backward angles; additionally, at any one angle, the magnitude of scattering can vary over 4 orders of magnitude in marine waters; (2) the magnitude of scattering is very low in the backward direction, particularly with respect to contaminating ambient solar flux in subsurface waters; and (3) accurate calibration protocols have been lacking.

[16] The Multiangle Scattering Optical Tool (MASCOT) measures the VSF using a 30 mW 658 nm laser diode source (World Star Tech model TECRL-30G-658) and 17 independent silicon diode detectors spaced from 10° to 170° in 10° increments relative to the incident beam (Figure 1). Sampling rate for all detectors is 20 Hz. The source beam is double folded and passes through a wedge depolarizer to provide highly collimated unpolarized incident irradiance. Independent detectors allow resolution of the VSF without any time-consuming moving parts, with each detector gain optimized for the dynamic range specifically observed at that angle. Detector field of views (FOVs) are set at 0.8°, 2°, 3°, and 4° for the 10°, 20°, 30°, and 40° measurements, respectively, to minimize smearing of the VSF in the steeply sloped forward portion while maintaining adequate signal based on relative nominal scattering intensities at specific angles. Keeping the FOVs as small as possible also avoids stray light contamination. Detectors at other angles have a FOV of 5°.

[17] Since a detailed account of the MASCOT calibration methodology has not been published previously, a full description is provided in Appendix A. The VSF of pure seawater was subtracted from measured $\beta(\theta)$ using the values of *Zhang et al.* [2009] to provide final $\beta_p(\theta)$.

3.4. Acoustical Bubble Measurements

[18] Bubbles respond strongly to sound because of their high compressibility, and consequently many different studies have used acoustical methods for bubble detection. Bubbles absorb and scatter sound most strongly at their natural frequency, which is largely determined by bubble radius. Consequently, a measurement of acoustical attenuation over a wide frequency range can be used to deduce bubble size distributions over a large radius range. An acoustical resonator consists of two steel-backed transducers, which face each other and are separated by about 25 cm [*Farmer et al.*, 1998]. The surrounding water can flow freely between the plates. One transducer produces broadband pseudorandom noise which is reflected back and forth between the transducers. The other transducer receives the summed signal from many reflections. The significant advantage of this technique is that the response consists of many simultaneous resonant peaks, caused when reflections constructively interfere. The resonator used for this study operated from 5 to 800 kHz, and a resonant peak was produced approximately every 4 kHz. This frequency range corresponds to a bubble radius range of 5–300 μm, although influence of geometrical scattering from larger bubbles, higher signal to noise, and uncertainty about the effect of bubble coatings can complicate interpretation for bubbles with radii below about 20 μm. Each peak provides a very sensitive measure of acoustical attenuation at that frequency, and so the output can be used to calculate the bubble size distribution present between the resonator plates during each measurement. In this case, a single measurement consisted of 0.25 s of acoustical data, and one measurement was made each second. The acoustical data was then inverted to get one bubble size distribution measurement each second. Further details of acoustical resonator operation are given by *Czerski et al.* [2011b]. The resonator was fixed adjacent to the MASCOT, with sample volumes separated by a distance of about 0.5 m.

3.5. Inversion Adaptation and Implementation

[19] The library of scattering functions for the inversion was built using subpopulations lognormally distributed with respect to size. A common assumption of early studies is that particle subpopulations all follow power law (Junge-type) distributions, which might be applicable to simplified one- or two-component models in some environments. The minimum and maximum size truncations of the Junge distribution, however, are hard to interpret [*Boss et al.*, 2001]. It is well known that the size distribution of phytoplankton species, one of the most optically significant and sometimes dominant constituents in the ocean, is lognormal [*Campbell*, 1995]. The lognormal distribution has also been used to characterize other living and nonliving individual populations including microbes [*Stramski and Kiefer*, 1991], detritus [*Longhurst et al.*, 1992; *Vaillancourt and Balch*,

2000; *Wells and Goldberg*, 1992; *Yamasaki et al.*, 1998], and mineral particles [*Jonasz*, 1987; *Lambert et al.*, 1981]. Theoretically, the natural processes of breakage [*Epstein*, 1947], coagulation [*Lai et al.*, 1972], or cell division [*Campbell and Yentsch*, 1989] would render a population of particles following the lognormal distribution [*Zhang et al.*, 2011]. Intuitively, we also know that at some small size particles transition into the dissolved phase, so having a model that reflects this is appealing.

[20] Relatively, and within their respective ranges of natural variability, the peak of a lognormal distribution and the real part of the refractive index exert the largest influence on the shape of the VSF, with the standard deviation of the lognormal distribution having a lesser impact. For a given peak size, slight differences in the shape of the size distribution, as represented by various possible models, have a minor effect on the shape of the VSF [*Zhang et al.*, 2011].

[21] Two libraries of phase functions were constructed to form the kernel in equation (1). The first modeled phase functions for resuspended quartz sediment assuming an asymmetric hexahedral shape using a combination of the discrete dipole approximation for small particles (<2 μm) and the improved geometric optics method for large particles. Phase functions for randomly oriented asymmetric hexahedra previously computed for the atmosphere [*Bi et al.*, 2010] were computed for the aquatic medium with a relative real refractive index of 1.16. The asymmetric hexahedral shape has sharp edges and corners with sides that are not exactly parallel, a more realistic representation than spherical or spheroid models. For these particles, radius is represented as a surface area equivalent sphere.

[22] This simple formulation contains no special case for scattering by mineral aggregates with a representative bulk refractive index less than 1.16 due to interstitial water. The lower bulk refractive index is likely less important than the relative shift in size distribution caused by aggregation. Diffraction at forward angles, which is weakly dependent on refractive index, would treat the aggregate as a single large particle, usually with less cross-sectional area than the combined cross-sectional area of the aggregated particles [*Boss et al.*, 2009; *Slade et al.*, 2011]. However, side and backscatter would be more representative of the individual particles comprising the aggregate if not too densely packed. Such aggregates in significant concentration would thus be expected to modify the inversion results, most likely by requiring two phase functions (one for particles the size of the aggregate and one for the particles making up the aggregate, both with refractive index of 1.16) to satisfactorily represent scattering by a single aggregate subpopulation.

[23] The other particle types considered in the model were bubbles, modeled as coated spheres with relative refractive index of 0.75, and "very small particles" (VSP), which represent a submicron size class where refractive index cannot be discriminated. The lognormal distribution was applied to every subpopulation. The VSP were modeled with 3 model radii (r_{mode} = 0.02, 0.04 and 0.08 μm) and 3 standard deviations (σ = 0.03, 0.05 and 0.07), with the phase function approaching isotropy as mean size decreases. For quartz sediment and bubble populations, each is modeled with 6 model radii (0.2, 0.4, 0.8, 1.6, 3.2, and 10 μm) and 4 standard deviations (from 0.1 to 1.0 at 0.3 interval). These values for modal radii and standard deviation encompass the optically significant particle range in the ocean and were determined based on a sensitivity analysis such that the resultant phase functions were uniformly spaced with respect to one another. Uniform spacing means that the wide range in the ratio of forward scattering to backscattering in phase function space ($\sim$0.5 for very small particles relative to wavelength up to 10^5 for very large particles) is well represented by the candidate subpopulations with no portion over- or underrepresented. Altogether, there were 57 potential candidates. Surfactant bubble coating thickness was assumed to be a constant 2 nm (M. L. Longo, personal communication, 2010) predominantly composed of lipids with a refractive index of 1.20. This coating thickness and refractive index are reasonable for surfactant molecules of lipid (e.g., fatty esters, fatty acids) and protein (e.g., glycoproteins, proteoglycans) composition [*Glazman*, 1983]. Resultant phase functions for bubbles and asymmetric hexahedra are plotted in Figure 2.

[24] Phase functions for the second library were all computed from Lorenz-Mie theory using an approach similar to that followed by *Zhang et al.* [2011]. Particle populations covered five particle refractive indices representative of bubbles and minerals (n = 0.75, 1.16, 1.18, 1.20, 1.22), 12 PSD modal radii, and 3 PSD standard deviations, giving 180 total permutations. In both libraries, a nominal imaginary refractive index of 0.002 was assigned to all subpopulations except bubbles. Note that this parameter has a negligible effect on inversion results unless the value is very high (>0.01) [*Twardowski et al.*, 2001; *Zhang et al.*, 2011].

[25] Because the phase function depends in a nonlinear manner on n, r_{mode}, and σ, it is possible that different particle subpopulations may produce a phase function of similar shape within the uncertainty of the measurements. These similar phase functions need to be removed to ensure the library (i.e., the kernel function) being constructed is neither singular nor pathological. An RMSE of 10%, or more than twice the expected uncertainty of the MASCOT VSF data (see Appendix A), was chosen as the singularity threshold (i.e., phase functions exhibiting RMSE differences greater than 10% relative to other phase functions were retained in the library). Within a group of subpopulations with phase functions that were too similar, the subpopulation with the phase function closest to the mean phase function was retained in the library. It is important to note that differences in composition among subpopulations that are optically similar are not dramatic; they are typically also very similar. For example, it is highly unlikely that subpopulations dominated by small particles and large particles would be similar optically. The inversion has been carried out by selecting other phase functions from within groups of similar subpopulations and any changes in the inversion results have been very minor. From the original library using asymmetric hexahedra for minerals, 35 phase functions were determined to be sufficiently unique to avoid singularities in the inversion from the fitting procedure (Figure 3). From the Lorenz-Mie theory library, 59 VSFs were determined to be sufficiently unique.

[26] Equation (1) was solved using a linear least squares algorithm with nonnegative constraints [*Lawson and Hanson*, 1974; *Portugal et al.*, 1994]. Since the variables to be determined were scattering coefficients that physically must be positive, the constraint of nonnegativity was

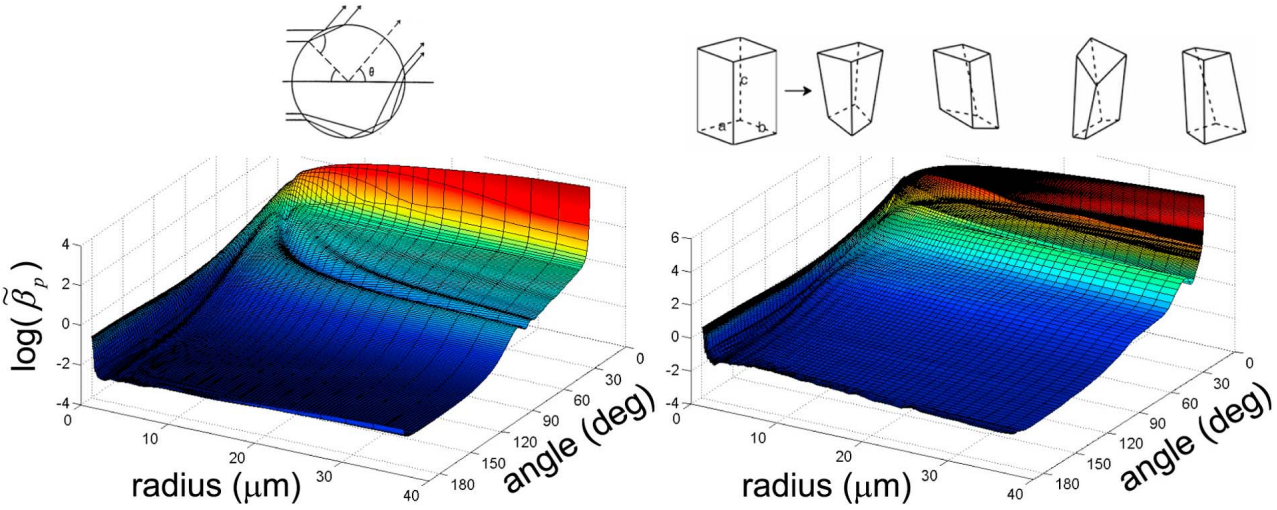

Figure 2. (left) Bubble and (right) asymmetric hexahedra phase functions used in the inversion library, $\lambda = 658$ nm. Particle shapes are shown above the phase function plots, with ray tracing demonstrating the midangle enhancement for spheres. Each bubble size is represented by a Gaussian distribution with standard deviation $0.2r$ to smooth high-frequency oscillations. The ridge of enhancement representing single internal reflections for bubbles approaches an asymptote of 83° for large particles. The less prominent secondary internal reflection ridge starts at a radius around 10 μm at an angle about 20° smaller than the primary, with the difference between primary and secondary ridges decreasing with increasing particle size. Asymmetric hexahedra are formed by starting with a rectangular box particle and then varying the length of edges labeled *a*, *b*, and *c* by random amounts [*Bi et al.*, 2010]. Randomly oriented asymmetric hexahedra phase functions are generally smooth at angles >30° with none of the rainbow reflections found for homogeneous spheres.

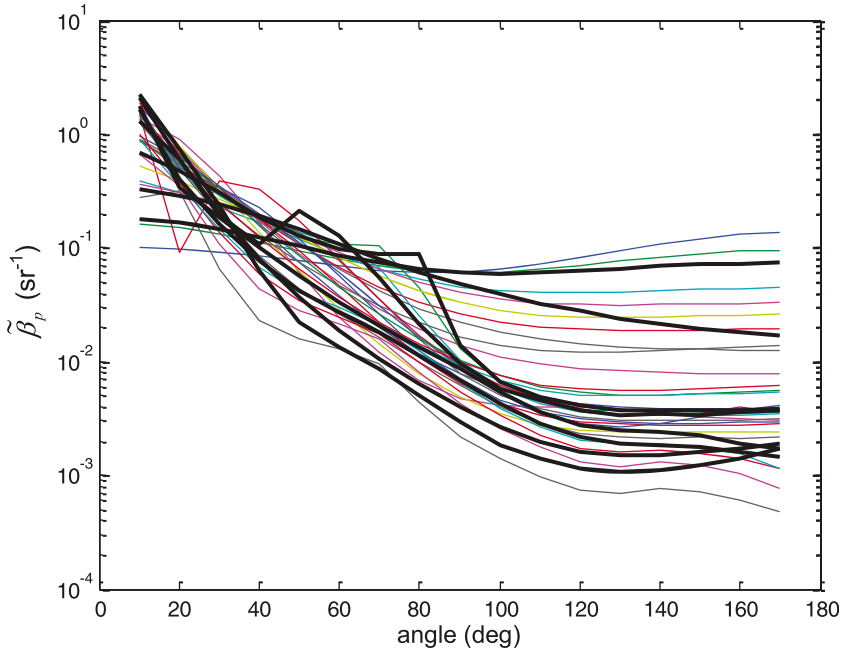

Figure 3. Plot of final 35 unique phase functions in library containing bubbles and asymmetric hexahedra representation of minerals for inversion. The eight that were picked by the inversion to explain the variability in the measured VSFs are in thick black.

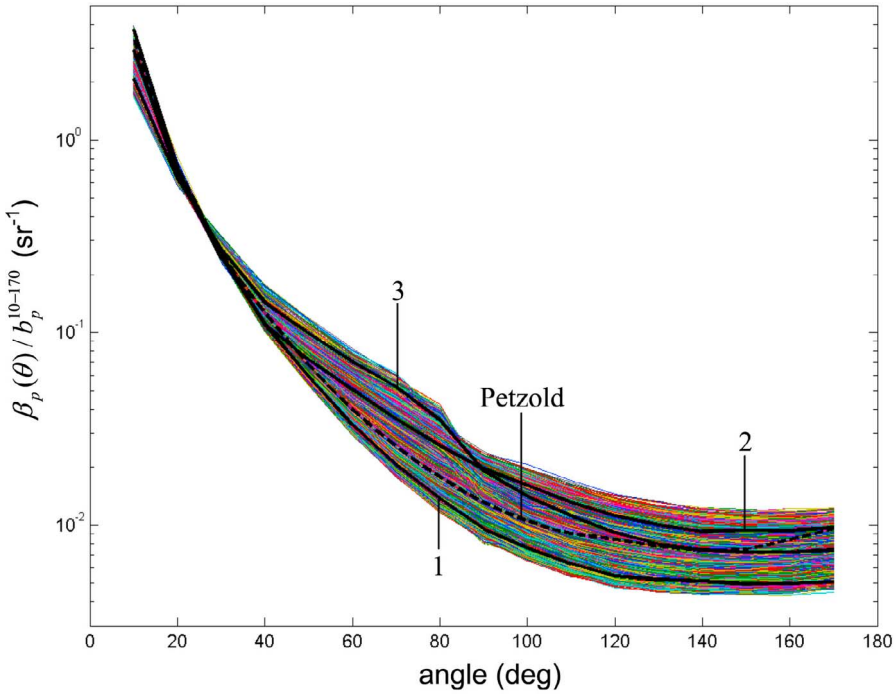

Figure 4. Variability in the shape of $\beta_p(\theta)$ from a 90 min MASCOT record collected off Scripp's Pier, 23 January 2008. The $\beta_p(\theta)$ is normalized to integrated particulate scattering between 10° and 170°, b_p^{10-170}. Data binned to 1 Hz (N = 5395). Bold traces marked 1, 2, and 3 are representative of the background (31.8 min in Figure 5), particles strongly influenced by suspended sediment (at 58.3 min in Figure 5), and water strongly influenced by bubbles (at 77.0 min in Figure 5), respectively. The dotted trace is the average of three measurements made by *Petzold* [1972] in San Diego Harbor, California.

employed to ensure physical soundness of the solution. If one of the derived b_i was zero, then the subpopulation associated with the corresponding VSF was assumed to have insignificant contribution.

4. Results

4.1. VSF Measurements

[27] A 90 min record of $\beta_p(\theta)$ was collected during ebb tide on 23 January 2008 starting at 10:59 local Pacific daylight savings time (Figures 4 and 5). The seaward edge of the surf zone was initially shoreward of the sensor package, gradually moving seaward with active wave breaking influencing the sensors after about 1 h (Figure 5). Starting bottom depth was approximately 2.5 m relative to mean sea level, decreasing to about 2.0 m by the end of sampling period. Faces of breakers averaged about 0.5 m. Three dominant $\beta_p(\theta)$ shapes were observed, representative of the background particle field, a particle field strongly influenced by bubbles, and a particle field strongly influenced by resuspended sediment (Figure 4). Other $\beta_p(\theta)$ shapes were composed of mixtures of these primary shapes. The midangle enhancement in $\beta_p(\theta)$ associated with relatively large (>∼5 μm) bubbles was clearly evident, consistent with theoretical predictions for spherical bubbles in seawater. Water with turbid patches of resuspended sediment showed enhanced backscattering ($\tilde{b}_{bp}^{10-170}$ = 7.8%) relative to the background condition ($\tilde{b}_{bp}^{10-170}$ = 3.9%), presumably due to the higher bulk refractive index associated with the sediment relative to the background particle field [*Twardowski et al.*, 2001].

[28] Normalized $\beta_p(\theta)$ data exhibited the least variability at approximately 25°, a region which was also intersected by the San Diego Harbor data from *Petzold* [1972] (Figure 4). This indicated that b_p^{10-170} may be estimated almost as well from a single β_p measurement at θ = 25° compared to measuring the entire β_p from 10° to 170° and integrating. Using the identity $b_p^{10-170} = 2\pi\ \chi\ \beta(25°)$ [see *Sullivan and Twardowski*, 2009], the resulting χ factor for these data was 0.39.

[29] Background $\beta_p(120°)$ values averaged 7 × 10^{-4} m^{-1} sr^{-1} (Figure 5, top), slightly more than an order of magnitude greater than scattering by pure seawater at 120° (6.15 × 10^{-5} m^{-1} sr^{-1}). For approximately the first hour of the record, background values were observed with periodic turbidity pulses peaking around 3, 21, 39, and 59 min. These turbidity patches were preceded by sets of larger waves which both enhanced sediment resuspension within the surf zone and extended the width of the surf into deeper water. Suspended sediment plumes associated with these wave sets breaking shoreward of our position on the pier were advected past the sensor package by a strong rip current running along the pier. The delay between a wave set breaking and the turbidity plume reaching the sensor package was roughly estimated at 1 min. As mentioned, these patches of suspended sediment had higher relative backscattering than the background (Figure 5, bottom) with a shape represented by the phase function marked "2" in Figure 4. After the first hour, strong increases in scattering

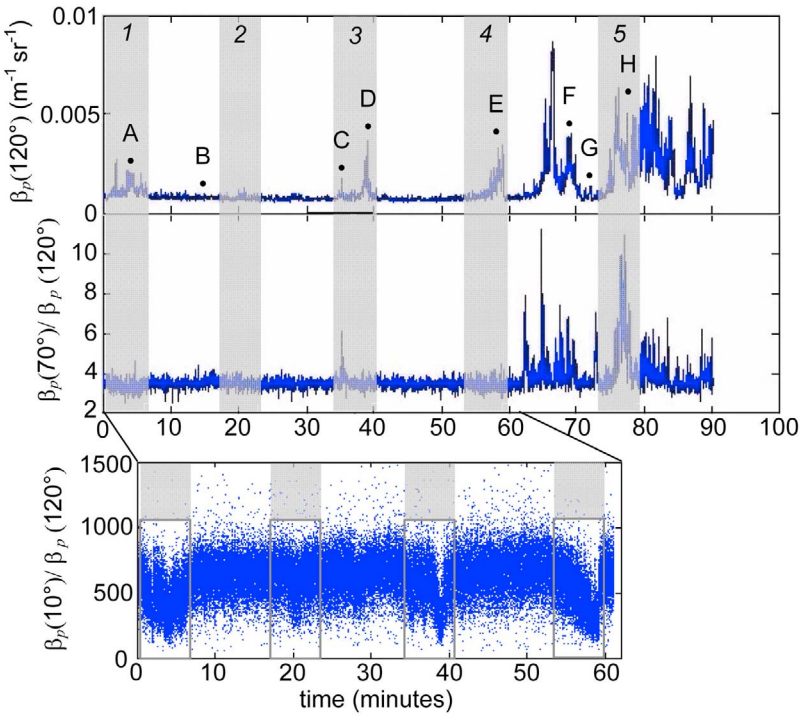

Figure 5. The (top) $\beta_p(120°)$ averaged to 1 Hz, (middle) $\beta_p(70°)$ / $\beta_p(120°)$ averaged to 1 Hz, and (bottom) full 20 Hz $\beta_p(10°)$ / $\beta_p(120°)$. Data collected during ebbing tide with surf zone gradually approaching sampling site. Wave sets, with time periods of 18–20 min, are shaded in light gray and labeled 1–5. Time periods marked A–H are used in subsequent analyses. VSF ratio $\beta_p(70°)$ / $\beta_p(120°)$ is expected to increase above the background in the presence of bubbles, while $\beta_p(10°)$ / $\beta_p(120°)$ is expected to decrease as the bulk refractive index of particles increases from the influence of resuspended sediments (see text for details).

were observed in association with local active wave breaking as the ebbing tide brought the surf zone within the location of the sensor package.

[30] The ratio $\beta_p(70°)$ / $\beta_p(120°)$ can serve as a proxy for the influence of bubbles greater than a few μm in diameter, as larger bubbles have enhanced scattering at $\beta_p(70°)$ relative to other types of particles (Figure 5, middle). Background values for the ratio were very stable around 3.5 for the first hour, indicating negligible influence from larger bubbles. The exception was a peak in the ratio at 35.4 min due to an isolated local breaking event outside the surf zone. After the first hour, local active wave breaking produced significant positive spiking in the ratio due to a strong influence from suspended bubbles formed by air injection and fragmentation following wave breaking.

4.2. Inversion Results

[31] MASCOT VSF data for the 90 min record were binned to 1 Hz (N = 5395) to effectively sample enough of the particle population to provide stable inversion results (see below). The optimal bin size depends on the particle density and size distribution and, through trial and error, inversion results at a 1 Hz sampling rate generally proved as stable as results averaging over larger bins. From the library that included asymmetric hexahedra and coated spheres representing mineral particles and bubbles, respectively, eight VSF shapes were picked in the inversion algorithm least squares minimization, including three bubble subpopulations, four mineral subpopulations, and a VSP subpopulation with radius 0.08 μm and standard deviation of log(r) of 0.3 where refractive index could not be reliably discriminated (Table 1). These eight phase functions could effectively describe the shapes of all the measured VSFs in the record, although only 4–5 were typically dominant for any one VSF.

[32] Time series of concentrations for the three most significant subpopulations showed a population dominated by sediment in the first hour of the record, followed by a period where sediment and bubbles were both present (Figure 6). Turbidity plume scattering peaks associated with wave sets

Table 1. Details of the Eight Particle Subpopulations Present in the Inversion Results With the Library Containing Asymmetric Hexahedra Representative of Mineral Particles

n	Radius, r (μm)	σ
utd[a]	0.08	0.3
0.75	0.2	0.1
0.75	3.2	0.1
0.75	10.0	1.1
1.16 + 0.002i	0.8	0.1
1.16 + 0.002i	0.8	0.4
1.16 + 0.002i	1.6	0.1
1.16 + 0.002i	1.6	0.4

[a]Here utd is unable to determine; VSP.

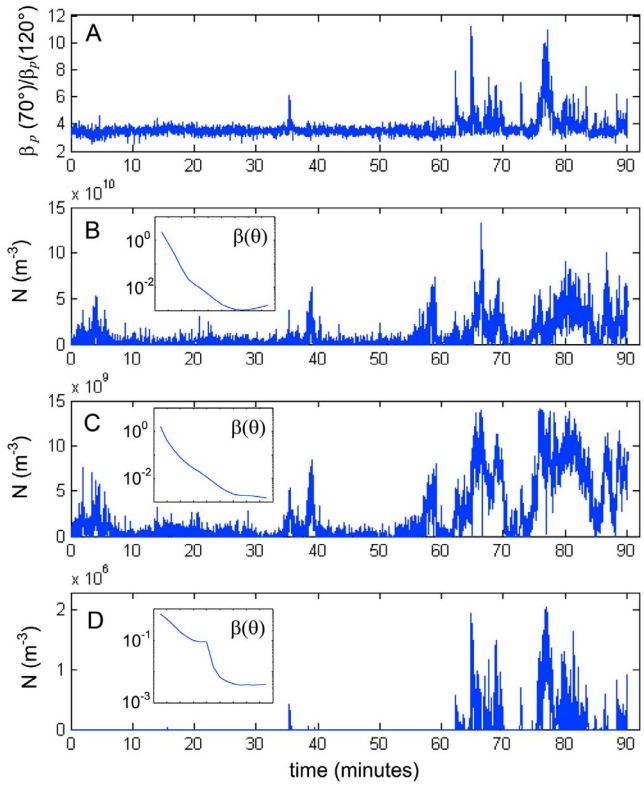

Figure 6. Time series of (a) $\beta_p(70°)$ / $\beta_p(120°)$, (b) dominant small sediment subpopulation concentrations (r = 0.8, σ = 0.1, n = 1.16), (c) dominant large sediment subpopulation concentrations (r = 1.6, σ = 0.4, n = 1.16), and (d) dominant large bubble subpopulation concentrations (r = 10, σ = 1.1, n = 0.75). Concentrations derived from library containing phase functions from bubbles and asymmetric hexahedra representing mineral particles. Representative phase functions for each subpopulation shown in insets with x axis ticks ranging from 20° to 160° in 20° increments.

1–4 (Figure 5, top) were clearly identified as sediment dominated in the inversion results (Figures 6b and 6c). The concentration time series for the large bubble subfraction (Figure 6d) appeared to correspond well to increases above the background in $\beta_p(70°)$ / $\beta_p(120°)$ (Figure 6a), including the spike at minute 35.4. Results including the spike agreed with anecdotal observations from time-resolved remote videography from the pier (data not shown) of the wave set turbidity plumes and local wave breaking during data collection.

[33] Eight examples of resulting size distributions from the inversion for combined bubble, mineral, and VSF subpopulations are shown in Figure 7. Size distributions for the background (Figures 7b and 7g) were dominated by the broad combined mineral component. In all of the distributions, the VSP and a small bubble component were always present in the inversion results and showed very consistent contributions. The only exception was during the period of local active wave breaking in the last half hour of the record, where sometimes (but not always) the VSP component was reduced (Figure 7h). This could be due to scavenging of VSP by injected bubbles, but may also be symptomatic of limitations in the inversion algorithm for these more turbid waters (see section 4.4 for discussion). Turbidity plumes associated with wave sets generally resulted in a broadening of the distribution for the mineral subfraction, including more of the larger particles (Figures 7a, 7d, and 7e). The size distribution associated with the isolated spike in the large bubble subpopulation at minute 35.4 (Figure 6d) is shown in Figure 7c. At times marked F and H there was evidence for a strengthening bubble subcomponent as the surf zone started to directly impact the location of the sensors. The influence was intermittent as might be expected, with periods showing a return to the background condition (Figure 7g). In specific size ranges with minimum radius in the range of 0.6 [*Groundwater et al.*, 2012] to 6 μm [*Buonassissi and Dierssen*, 2010], the Junge-type power law model provided a reasonable fit to aggregate distributions, with slopes between 3 and 4, typical of natural oceanic distributions [*Kitchen*, 1977; *Buonassissi and Dierssen*, 2010; *Groundwater et al.*, 2012].

[34] The ostensible covariation of $\beta_p(70°)$ / $\beta_p(120°)$ and the concentration of the large bubble subcomponent obtained from inversion suggested that $\beta_p(70°)$ / $\beta_p(120°)$ may be able to serve as a simple proxy for this subfraction (Figure 8). While the correlation coefficient was 0.69 with a quadratic fit, residual errors in using $\beta_p(70°)$ / $\beta_p(120°)$ as a proxy would still be large, although perhaps still tolerable for many applications.

[35] Coincident measurements with an acoustical resonator [*Farmer et al.*, 1998; *Czerski et al.*, 2011b] showed good agreement with the large bubble subpopulation derived from inversion (Figure 9), providing good cross validation between the techniques. Acoustical resonators typically resolve bubbles greater than about 20 μm radius, although recent work has demonstrated the ability to quantify smaller bubbles that significantly impact seawater optical scattering [*Czerski et al.*, 2011a].

4.3. Comparison to Results Assuming Homogeneous Spherical Populations

[36] From the library containing only homogeneous spherical particles and coated spheres, 18 VSF shapes in total were picked in the inversion algorithm least squares minimization to describe the shapes of all the measured VSFs in the record (Table 2), with 5–10 typically picked for any single VSF measurement. Time series for the dominant sediment and bubble subpopulations derived from inversion are shown in Figure 10. Note the concentrations for the sediment subpopulation were higher than those for the subpopulations shown in Figure 6 because they represent a smaller mean size class. Bubble subpopulations and the mineral subpopulations with n = 1.16 accounted for more than 90% of the VSF in all cases, with the n = 1.18 and n = 1.22 subpopulations picked by the inversion always providing very minor contributions. The significant mineral subpopulations that were picked were composed of relatively small size distributions without rainbow effects in the backward portion of the phase function (i.e., intensity peaks due to lensing effects observed with perfectly spherical particles). While the time series of the mineral subpopulations had features that were relatively consistent with results obtained with the library representing minerals as asymmetric hexahedra, the bubble subpopulations were noisier and showed evidence for sediment signal incorrectly

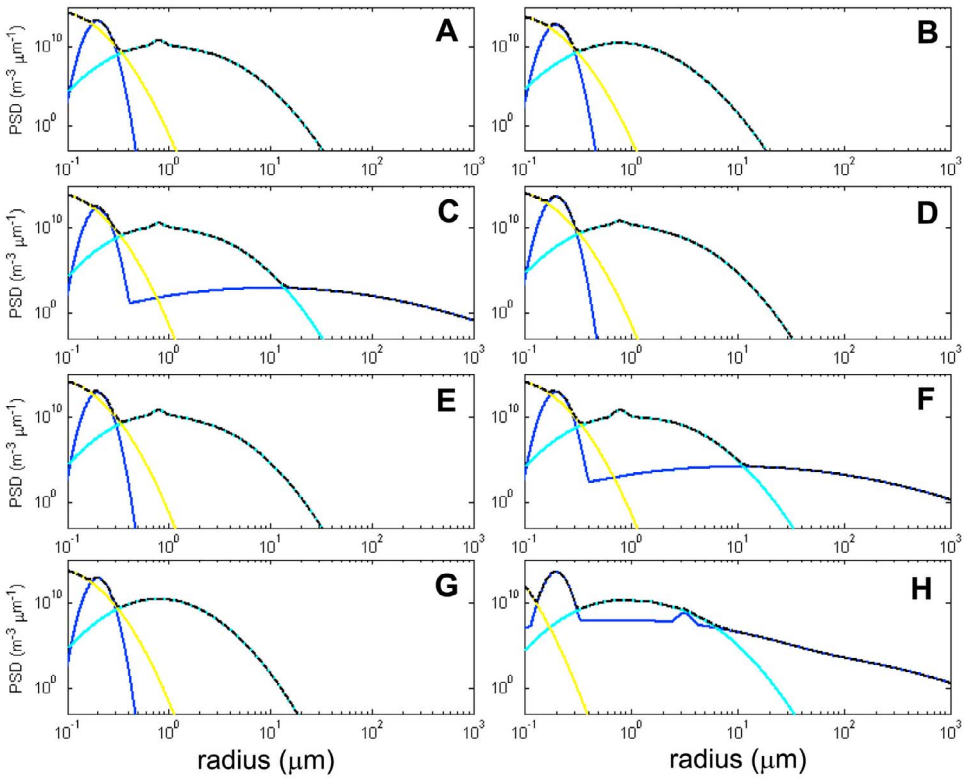

Figure 7. Particle size distributions solved from the inversion. (a–h) Plots correspond to marked locations in Figure 5. Yellow trace is VSP, purple trace is combined bubble subpopulations, cyan trace is combined mineral subpopulations, and dotted trace is total.

assigned to bubble subpopulations. This resulted primarily because Lorenz-Mie theory modeling of phase functions for larger mineral subfractions show the unrealistic rainbow peaks that are not observed in natural VSFs. The algorithm thus tries to accommodate increased backscattering due to minerals by fitting phase functions from coated bubbles that also show elevated backscattering. The result is somewhat ironic since one might reasonably expect the bubble subfractions to be represented well in inversion results for a library composed of exclusively spherical particles. Overall,

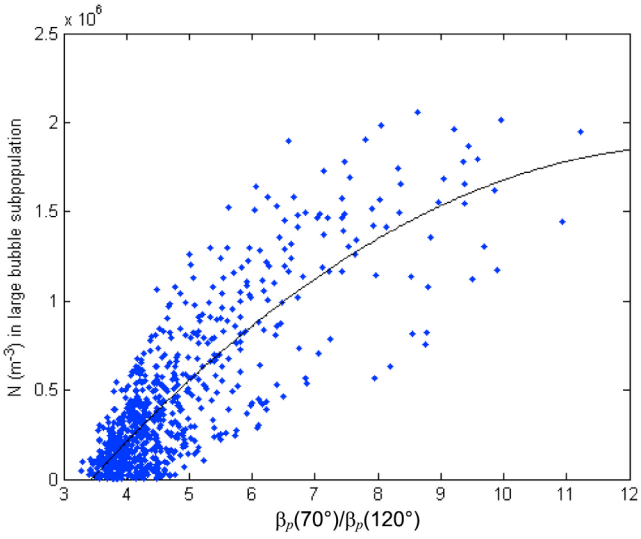

Figure 8. The $\beta_p(70°) / \beta_p(120°)$ as a proxy for the concentration of large bubbles solved through the inversion. Quadratic fit $Ax^2 + Bx + C$ has coefficients $A = -2.00\ 10^4$, $B = 5.25\ 10^5$, and $C = -1.57\ 10^6$ with $r^2 = 0.69$.

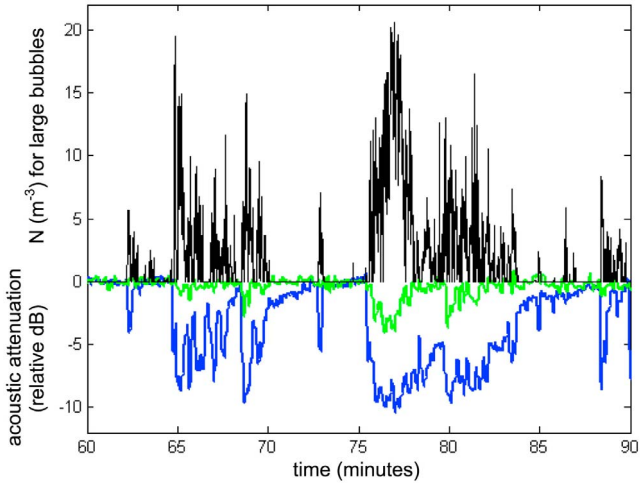

Figure 9. Large bubble subpopulation from inversion (black trace) and relative attenuation in sound wave transmission due to bubbles at two frequencies from an acoustical resonator. The frequencies of the blue and green traces (23 and 10 kHz) correspond to resonant bubble radii of 143 and 332 um, respectively.

Table 2. Details of the 18 Particle Subpopulations Present in the Inversion Results With the Library Containing All Homogeneous Spheres and Coated Spheres

n	Radius, r (μm)	σ
0.7500	0.0200	0.2000
0.7500	0.2000	0.2000
0.7500	0.4000	0.2000
0.7500	0.4000	0.4000
0.7500	2.0000	0.6000
1.1600 + 0.001i	0.0600	0.6000
1.1600 + 0.001i	0.1000	0.2000
1.1600 + 0.001i	0.1000	0.4000
1.1600 + 0.001i	0.1000	0.6000
1.1600 + 0.001i	0.4000	0.2000
1.1600 + 0.001i	0.4000	0.4000
1.1600 + 0.001i	0.6000	0.2000
1.1600 + 0.001i	0.6000	0.4000
1.1600 + 0.001i	3.0000	0.6000
1.1800 + 0.001i	0.6000	0.2000
1.2200 + 0.001i	0.1000	0.6000
1.2200 + 0.001i	0.4000	0.2000

inversion results are much less stable (see below) than observed with the library representing minerals as asymmetric hexahedra, with more subpopulations picked per VSF, and more variability in the composition of subpopulations from VSF to VSF.

4.4. Inversion Stability

[37] The relative stability of the inversion is most evident in the consistency of results. The high sampling rate of the MASCOT sensor provides a large sample size with which to evaluate stability. A detailed sensitivity analysis for the method is provided by *Zhang et al.* [2011] and is considered here as it pertains to these inversion results. Inversion stability can be gauged in two ways: algorithm stability and performance stability. To evaluate the algorithm stability, the inversion was run twice: first with full candidate phase functions and second with only those candidate phase functions picked by the inversion from the first run. The inversion results proved to be the same between the two runs, suggesting that the inversion algorithm is stable and the solutions obtained are unique. This also suggests that the inclusion of nonrealistic subpopulations will not distort the results. Libraries with different groupings of the size parameters r_{mode} and σ were also tested and inversion results converged on the same solutions as long as the full ranges of size distributions were included. RMSEs between measured VSFs and aggregate VSFs resulting from the least squares minimization in the inversion algorithm were always <1% for both phase function library kernels tested.

[38] Performance stability measures the overall performance of the inversion when random noises are introduced to the inputs. This can be evaluated by examining if consistent results can be obtained when the water being sampled was effectively invariant over a specific time period, or, in other words, when the VSFs measured only showed variation beyond electronic noise from random contributions from a particle population comprising a stable background condition. An example of such a situation is during the first 60 min or so when a stable background was sampled between turbidity plumes associated with wave sets (Figure 5). Subpopulation contributions should remain roughly constant through these time periods. One obvious indication of stability was the consistent absence of large bubbles (represented by $r = 10$ μm and $\sigma = 1.1$) in the first hour except for the single injection event at 35.4 min (Figure 6d), which was a real feature confirmed visually.

[39] Variability in subpopulation contributions can be represented as $S = \sum_{i=1}^{M} \sigma_{b_i} / M$, or the sum of the standard deviations in contribution to total particle scattering of each subpopulation (b_i in equation (1)) picked by the inversion. This parameter can be used to evaluate inversion stability during consistent periods of background sampling, where the same subpopulations would be expected to be present with consistent contributions and S should therefore be relatively small. In inversion results from periods sampling a constant background in the first hour of the record, S was 0.0046 for the library with asymmetric hexahedra representing minerals and was 0.0082 for the library with spherical representations only. The higher S value is a reflection of a high degree of variability in the dominant subpopulations. Note that S is not an assessment of inversion accuracy necessarily, but stability, as a result could be consistently wrong (biased), as with some bubble contributions in the inversion with the spherical subpopulation library.

[40] Inversion accuracy and stability are not independent of one another, however; factors that degrade both can be summed up as the so-called GIGO (Garbage In, Garbage Out). If the subpopulation phase functions in the kernel library are not representative, both accuracy and stability will suffer, and better stability typically indicates a more accurate inversion. Problems with the inversion can also be readily apparent with a relatively simple optical case such as Scripps Pier where only two major particle types dominate. Errors in solving for one particle type are immediately

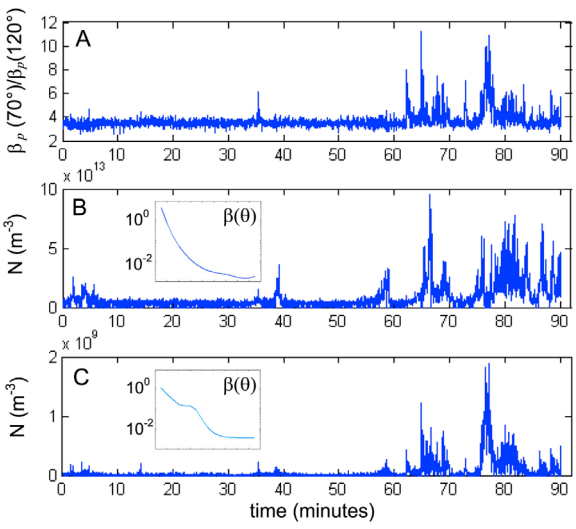

Figure 10. Time series of (a) $\beta_p(70°) / \beta_p(120°)$, (b) dominant sediment subpopulation concentrations (r = 0.2, σ = 0.1, n = 1.16), and (c) dominant bubble subpopulation concentrations (r = 2.0, σ = 0.6, n = 0.75). Concentrations derived from inversion using library with exclusively homogeneous spherical particles. Representative phase functions for each subpopulation shown in insets with x axis ticks ranging from 20° to 160° in 20° increments.

revealed in results for the other particle type. In a more complex environment such as the New Jersey coast, where a multitude of particle groups may have significant contributions, the spherical assumption may not affect a specific subpopulation in the inversion results as strongly as observed in this study [*Zhang et al.*, 2011].

5. Discussion

[41] Consistent with the physical dynamics of the surf zone, the shape and magnitude of the volume scattering function varied substantially over short time scales during a 90 min collection period that included conditions outside, bordering, and within the surf zone (Figure 5). VSF magnitude varied about an order of magnitude, with highest values observed under localized wave breaking with simultaneous bubble injection and sediment resuspension. With respect to shape, normalized VSFs spanned up to a factor of 3 in total range at any one angle, with the greatest variability from 60° to 80° where the enhancement due to bubbles is prominent (Figure 4). Similar observations have been made with the MASCOT device deployed in the subsurface of Santa Barbara Channel (M. Twardowski, unpublished data, 2008), the Southern Ocean (K. Randolph et al., Optical measurements of bubble size distributions at 6–9 m depths generated by large-scale breaking waves in the Southern Ocean, manuscript in preparation, 2011) and south of Hawaii [*Czerski et al.*, 2011a] during periods of wind driven wave breaking. To our knowledge, these are the first in situ oceanic measurements verifying the theoretically predicted midangle enhancement in bubble phase functions.

[42] Considering the observed variability in VSF shape and also the variety of possible shapes of the particulate VSF due to different assemblages of background particles in the surface ocean, assuming VSF shapes in modeling radiance distributions in near-surface waters will likely lead to significant errors. This is likely not the case, however, when considering only the backward portion of the VSF (Figure 4), which has been shown to be quite consistent in its general shape over a broad range of oceanic water types (*Sullivan and Twardowski*'s [2009] analysis included the data presented here). Thus, modeling upwelling radiance distributions when the solar zenith and viewing angle are near nadir is expected to be a case where assuming VSF shapes is likely justified without very significant error. Because of beam refraction, this assumption is likely valid over a range of angles extending beyond 45° relative to nadir. It should be noted that despite the consistency in the general shape, variability in the shape of the backward VSF, particularly near 90° and 170°, was still observed in this study and was significantly greater than our signal-to-noise, which aided in discrimination of subpopulations by the inversion.

[43] Using the shape of the VSF between 10° and 170° to derive size distributions and composition of particle subpopulations provides advantages relative to other particle characterization techniques. Several approaches for resolving size distributions are available, although none provide any systematic information on particle composition except scanning electron microscopy coupled with an energy dispersive spectrometer [*Peng et al.*, 2002, 2007; *Groundwater et al.*, 2012]. All of these techniques require discrete sample collection and suffer associated limitations [*Gardner et al.*, 1993; *Twardowski et al.*, 2005] except for in situ adaptations of laser diffractometry [*Agrawal and Pottsmith*, 2000]. For in situ sampling of bubble size distributions only, the acoustical resonator [*Farmer et al.*, 1998; *Czerski et al.*, 2011b] and videography [*Deane and Stokes*, 1999] have been the most popular approaches, although lower size limits are several and 80 μm, respectively. Optical scattering is the only technique we are aware of that is capable of discriminating bubble size distributions below several microns into the colloidal domain. This is the size range that would include the hypothesized "persistent bubbles" in the ocean, which may serve as nuclei for cavitation phenomena [*Yount et al.*, 1984; *Zhang et al.*, 2002] (further discussion below).

[44] One promising approach for particle characterization that has been scarcely employed in the past because of the enormous quantities of data generated is in situ holographic microscopy, which can now provide instantaneous 3-D digital images of optically relevant particles in unperturbed water [*Pfitsch et al.*, 2005; *Talapatra et al.*, 2010]. Determination of size distributions grouped according to particle shape can now be carried out from digital images in automated analyses in time periods of minutes. Spherical particles such as bubbles can be identified using the Hough transform and quantified within a complex particle assemblage [*Katz*, 1978; *Ran and Katz*, 1991]. So whereas the inversion approach described here can provide refractive index distributions, microscopic holography can provide complementary distributions of similarly shaped particles.

[45] Near-forward diffraction scattering (laser diffractometry) can resolve size distributions for particle sizes greater than $\sim$2–10λ [*Buonassissi and Dierssen*, 2010; *Reynolds et al.*, 2010], but these include all particles without any information on population composition. Refraction and reflection effects present in larger angle scattering provide information on particle composition in addition to size. From particle composition, manifested optically in refractive index distributions, particle density distributions can readily be derived [*Carder et al.*, 1974; *Aas*, 1981]. With these results in hand, a host of particle biogeochemical properties may then potentially be determined quantitatively, including total suspended matter, particulate organic matter, particulate inorganic matter, and particle settling rates. Optical properties have been used as empirical proxies for these parameters in the past, but results were only valid assuming the composition of the particle population was relatively constant. The inversion technique described here is analytical and requires no such assumptions.

[46] Inversion results using the library with asymmetric hexahedra phase functions representing mineral particles provided consistently stable results that agreed anecdotally with qualitative videography observations made from the pier. A high sampling rate and subsequently large numbers of observations was essential in evaluating inversion stability. Concentrations of large bubbles under breaking waves were consistent with previous measurements using acoustical [*Baldy*, 1988; *Cartmill and Su*, 1993; *Farmer et al.*, 1998; *Terrill et al.*, 2001] and videography [*Deane and Stokes*, 1999, 2002] techniques. The large bubble subpopulation from the inversion showed a distribution consistent with large bubbles resolved with an acoustical

resonator (Figure 9). A direct quantitative comparison of bubble size distributions south of Hawaii derived from acoustical resonator measurements and the inversion of optical scattering as described here was also very encouraging [*Czerski et al.*, 2011a]. Aggregate particle size distributions from all subpopulations picked by the inversion also could be modeled well ($r^2 > 0.9$) with the commonly observed Junge-type power law distribution when minimum radii used in previous studies were considered. Slopes of the fit were consistent with values reported in the literature [*Kitchen*, 1977; *Buonassissi and Dierssen*, 2010; *Groundwater et al.*, 2012]. Moreover, available evidence suggests the correct subpopulations were picked by the inversion and that their relative concentrations fell within reasonable ranges.

[47] For the library with phase functions of all particles modeled as spheres, inversion results were skewed because key subpopulations, specifically mineral groups including substantial relative concentrations of larger particle sizes ($>\sim$20 μm), effectively could not be picked by the algorithm because they exhibited unrealistic rainbow (spherical lensing) effects in the phase function. The inversion was therefore more unstable, with some bubble subpopulations in the results accounting for large mineral particle scattering. Nonetheless, some agreement was observed in the distributions of the dominant sediment and bubble subpopulations for both the spherical and nonspherical libraries tested (Figures 6 and 10).

[48] Certainly a large contributor to the success of the randomly oriented asymmetric hexahedra representation for minerals in the inversion was simply the lack of any rainbow effects in the backward portion of the phase function. One implication of this result is that the phase function of other nonspherical particles with very complex shape, such as the majority of phytoplankton, might be represented to first order using any randomly oriented complex shaped particle with the same scattering cross section (defined as the area where the impinging energy from the incident wave is equal to the total energy scattered in all directions). In other words, phase functions for many randomly oriented very complex shaped particles of the same scattering cross section *may* be similar enough to effectively solve for their scattering cross section via inversion. Scattering cross section and the lack of unrealistic rainbow effects at least appear to be important first-order determinants. The observation that the general shape of VSFs measured in natural waters has relatively consistent features in a wide variety of different water types (monotonically decreasing with increasing angle, relatively flat in the backward direction, steeply peaked in the forward direction, a minimum around 140°) may suggest that structural complexity in natural particles has a "homogenizing" effect on phase function shapes. Degree of complexity must be a consideration, as many simple nonspherical shapes and structures will have unique phase functions when randomly oriented in solution [*Mishchenko et al.*, 2000; *Clavano et al.*, 2007], although such particles would be considered rare in natural waters. Particle structures as complex as coccoliths and assemblages of coccolithophorids have a VSF shape similar to that of oceanic VSFs [*Voss et al.*, 1998], although obtaining cultures with minimal background particle contamination from detrital matter and microbes is difficult. Characterizing the level of variability in the phase functions of complex particles requires further investigation.

[49] One intriguing phenomenon that may be evaluated with the inversion results is the so-called "persistent bubble hypothesis" [*Zhang et al.*, 2002], where a constant background population of submicron bubbles is postulated to exist throughout the ocean, presumed to be the source for larger bubbles produced by cavitation [*Yount et al.*, 1984]. These bubble nuclei are thought to be stabilized with organic surfactant film that inhibit diffusion into solution and provide a surface mass that maintains neutral buoyancy. On the basis of optical scattering measurements off the coast of New Jersey, *Zhang et al.* [2002] concluded that up to 40% of backscattering could be attributed to persistent submicron bubbles. If true, this would have vast implications for ocean color remote sensing and solar transmission in general through the ocean's subsurface.

[50] The existence of a persistent submicron bubble background throughout the ocean is challenged by several observations. First, if these bubbles are persistent (presumably on time scales at least greater than hours) and produced and maintained by air injection from wave breaking and associated jet and drop entrainment [*Deane and Stokes*, 2002], then their concentrations should sequentially increase with each breaking wave event. Scattering measurements in the surf zone and subsurface ocean during whitecapping have not shown any such increase in background scattering over time. There is also no consistent decrease in optical scattering with depth in the ocean, as may be expected due to (1) pressure effects reducing the background bubble geometric cross section and (2) increasing distance from the source of generation at the surface. Also, in the very clearest oceans, scattering levels in the backward direction approach that for pure seawater [*Twardowski et al.*, 2007]. Even *Zhang et al.* [2002] concede that "the existence of such small bubbles is questionable…," partly based on the fact that direct observations are lacking.

[51] In spite of the conceptual conflicts with the hypothesis, a constant submicron bubble subpopulation background was observed in the inversion results in all of the different water types sampled during the 90 min record (Figure 7). This subpopulation can be discriminated from the VSP subpopulation because the organic coating results in elevated relative backscattering. It is interesting to note that the colloidal VSP subpopulation was also essentially constant, with larger mineral and bubble subpopulation concentrations modulating over this background. While an isolated single set of measurements, these observations appear consistent with a persistent submicron bubble population without resolving any of the conceptual conflicts, suggesting further study is warranted.

[52] Ongoing work with the inversion algorithm includes adding near-forward diffraction scattering to the large angle MASCOT scattering measurements to improve details in derived particle size distributions [*Agrawal and Pottsmith*, 2000], adding recent measurements of polarized scattering made with the MASCOT [*You et al.*, 2011b], and continuing to expand the use of representative nonspherical shapes in phase function libraries. Adapting inversion results to serve as a comprehensive tool for deriving particle biogeochemical parameters is also a current focus. By providing the information needed to better understand subsurface particle

dynamics, it is expected that inversion results can be useful in developing models in the future to forecast subsurface optical properties based on climatology and physical forcing variables.

Appendix A: MASCOT VSF Calibration

[53] To calibrate each of the 17 raw signals to volume scattering coefficients, $\beta(\theta)$ (m^{-1} sr^{-1}), a dark offset D must be subtracted from the raw digital counts Φ and the result multiplied by a scaling factor and attenuation correction

$$\beta(\bar{\theta}_i) = \frac{R_{\mathrm{cal}}}{R_m}[\Phi_i - D_i] f_i e^{L\left[b_p\varepsilon + a_{pg} + a_w\right]}, \quad \text{(A1)}$$

where f is the scaling factor related to detector gain with units m^{-1} sr^{-1} $counts^{-1}$, the R parameters are source reference counts recorded during the calibration when determining f (subscript cal) and during the in situ measurement (subscript m), L is the path length (distance from source window to sample volume to detector window, which is nominally 20 cm for each scattering measurement), ε is the fraction of scattering by particles that is not included in the measurement (i.e., the scattered fraction that is not within the acceptance window of the sample volume and detector, see below), b_p is the particulate scattering coefficient, a_{pg} is the absorption by particulate and dissolved material, and a_w is the absorption coefficient for pure water from *Pope and Fry* [1997]. Note that ε can be represented by an angular weighting function and will be dependent on the phase function of the particle population. The scattering and absorption coefficients are specific to λ = 658 nm. For a stable source, the R terms should be approximately equal. The exponential term is a correction for attenuation loss along the path of the scattering measurement, where ε must fall in the range 0–1. The effects of molecular scattering are ignored in this correction, as they are negligible relative to the other coefficients. The i subscript represents the 17 individual channels. The bar over θ signifies the centroid angle of the specific angular weighting for the ith scattering measurement.

[54] There are effectively three parameters in equation (A1) that need to be derived in calibration: D, f, and ε. The following method for calibration is similar to that used by WET Labs for the ECO sensor series [*Twardowski et al.*, 2007; *Sullivan et al.*, 2012], with the primary difference being that the longer path length of the MASCOT scattering measurements requires a more rigorous attenuation correction.

[55] Dark offsets D were obtained in situ in the field by placing black tape over the source. No dependency on temperature was observed, with dark offsets usually showing less than 1% standard deviation during a time series measurement, so that the entire record could be averaged to obtain D. In situ dark offsets were collected immediately after or before a standard ambient scattering measurement, ensuring the most accurate correction possible.

[56] The first step in calibration is rewriting equation (A1) in terms of a known standard. This is necessary since there are currently no standard solutions with reproducible $\beta(\theta)$. Solutions of known phase function $\tilde{\beta}_p(\theta) = [\beta_p(\theta) / b_p]$ (sr^{-1}) can be prepared however from microspherical beads with size distributions traceable to NIST standards. The phase function may be computed using Lorenz-Mie theory if the bead size distribution and refractive index are known. Since b_p can be measured directly during calibration using a WET Labs ac9, $\beta_p(\theta)$ may then be obtained for any concentration of beads. Substituting into equation (A1), removing the R terms (R_{cal} must be recorded for use later in applying equation (A1) to in situ data), and solving for $[\Phi - D]$ we obtain

$$[\Phi_i - D_i] = b_p \frac{\tilde{\beta}(\bar{\theta}_i)}{f_i} e^{-L\left[b_p\varepsilon + a_{pg} + a_w\right]} = b_p M_i e^{-L\left[b_p\varepsilon + a_{pg} + a_w\right]}, \quad \text{(A2)}$$

where $M = \tilde{\beta}_p(\bar{\theta}) / f$ (counts m). In theory, M and ε could be solved for each scattering measurement using a least squares minimization of residuals to experimental data of measured counts Φ and b_p in a solution with known phase function $\tilde{\beta}_p(\bar{\theta})$. Although this method can be effective, we can achieve better accuracy with the knowledge that ε should be approximately the same for all the 17 scattering channels because the detector footprints and the cross-sectional area of the sample volumes with respect to the incident beam are all approximately equal. These are the characteristics of the measurement geometry that primarily define ε. Thus, the shape or curvature of the relationship between Φ and b_p for each of the different channels should be very similar.

[57] As mentioned, ε is characterized by an associated angular weighting function and thus will change as the particle phase function changes. As a result, the test particle standard known as Arizona Test Dust (ISO Ultrafine ATD 12103–1, Powder Technologies, Inc.) was used to empirically obtain ε, as ATD has a broad size distribution that is modeled well by a power law (differential Junge-type) for particles less than about 6 μm. Its phase function is similar to natural phase functions for randomly shaped sediment particles [e.g., *Agrawal and Mikkelsen*, 2009]. From a suspension series of ATD, ε was solved by normalizing the signal response for each scattering channel as a function of b_p to the area under the curve (essentially removing the M_i gain effect for each channel since the integrated area is $M_i \int b_p e^{-L[b_p\varepsilon + a_{pg} + a_w]} db_p$), and then least squares fitting the combined results for all channels to equation (A2) (Figure A1). The resulting ε was 0.56, indicating that 44% of light scattered by particles fell within the solid angle defined by the detector footprint (for light traveling from the sample volume toward the detector) and the sample volume (for light traveling from the source to the sample volume). Because of the relatively strong absorption by water at 658 nm (0.396 m^{-1}), a large uncertainty in ε will have a negligible uncertainty (<1%) in the overall attenuation correction in clear waters. As an example in more turbid waters, for b_p around 2 m^{-1} a 20% uncertainty in ε will result in about a 5% uncertainty in the attenuation correction.

[58] There are two important notes with respect to this method of deriving ε. First, we cannot assume b_p is equivalent to measured c_p from an ac9 for ATD; even though ATD is known to have a relatively small absorption, it is not negligible [*Egan*, 1982]. The ac9 absorption measurement requires a scattering correction, which was estimated at 10% of b_p based on applying the angular weighting function for the scattering error of the ac9 absorption tube derived by *McKee et al.* [2008] to the phase function for ATD.

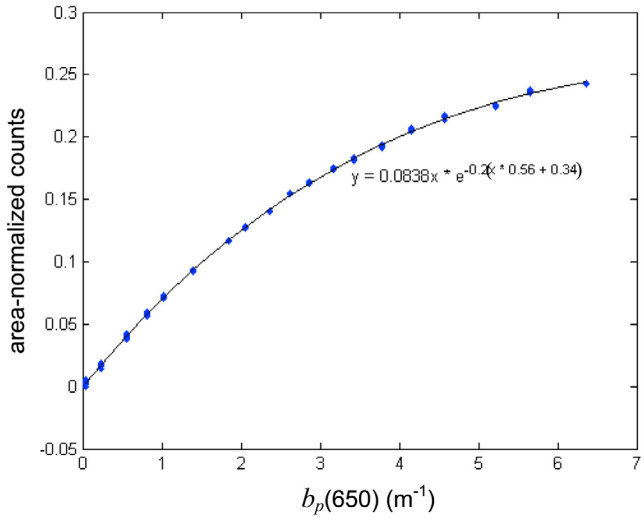

Figure A1. Raw digital counts for all 17 MASCOT detector channels as a function of $b_p(650)$, normalized to area under the curve (see text). Normalization removes the effects of different gain settings for the different channels, as we are only interested in the shape of the curve in determining a correction for path attenuation. Fitting equation (A2) to these data gives the solution 0.56 for the ε parameter (see text for details).

Knowing that $b_p = c_p - a_{\text{"true"}}$, and that $a_{\text{"true"}} = a_{\text{meas}} - 0.1\, b_p$, we can substitute to obtain $b_p = (c_p - a_{\text{meas}}) / 0.9$. The second point is that b_p evaluated with an ac9 transmission measurement is in fact $\beta(\theta)$ integrated from 0.93° to 180° because the ac9 acceptance angle is 0.93°. Because of steeply sloped natural phase functions in the near-forward, true b_p will be underestimated with an ac9-measured b_p, the degree to which will depend on the phase function shape. Thus, the derived ε is specific to b_p derived from a transmissometer with a 0.93° acceptance for scattered light.

[59] With ε in hand, M_i parameters were derived from experimental measurements in a suspension series of particles with precisely known phase function $\tilde{\beta}_p(\theta_\iota)$ so that scaling factors f_i could subsequently be computed. The parameter M_i was solved individually for each channel using a least squares minimization of the model in equation (A2). NIST-traceable polystyrene microspherical beads with modal diameter 0.1998 ± 0.0006 μm and standard deviation 0.0034 μm were used for calibration (size parameters were reported by the manufacturer, Duke Scientific, Inc., now ThermoScientific). These relatively small bead particles were chosen because, in general, the smaller the particle the lower the sensitivity to uncertainties in size distribution parameters (including any clumping), refractive index (both real and imaginary), and the angular weighting of the scattering measurement. The ε parameter derived as described above with ATD could not be applied here, as ε should be much higher with a phase function for small particles close to the Rayleigh scattering regime. Consequently, the dynamic range for these calibrations was capped at b_p levels of approximately 0.2 m^{-1} to minimize the attenuation correction effect, and ε was roughly estimated as 0.8. The resulting correction was dominated by water absorption and was about 10% for all bead concentration levels. Even with a ±0.2 uncertainty in the ε that was used, the resulting uncertainty in the attenuation correction was less than 1% at these b_p levels.

[60] With M_i values in hand, scaling factors f_i can be derived from computed $\tilde{\beta}_p$ for the beads. A phase function $\tilde{\beta}_p$

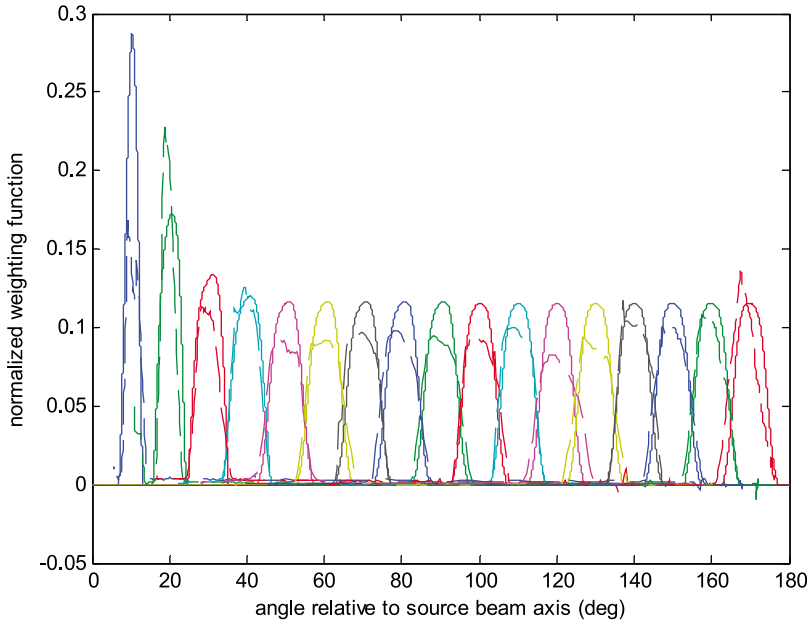

Figure A2. Angular weighting functions for the 17 MASCOT VSF channels. Solid traces were computed numerically, and dotted traces were derived from lab measurements in air.

for the bead solution weighted to the angular response $W(\theta)$ for each of the MASCOT scattering measurements is fully represented as

$$\frac{\beta_p(\bar{\lambda},\sigma_\lambda,\bar{\theta},\Delta\theta,\bar{d},\sigma_d)}{b_p(\bar{\lambda},\sigma_\lambda,\bar{d},\sigma_d)}=\frac{\int_0^{\pi}\int_{\bar{\lambda}-3\sigma_\lambda}^{\bar{\lambda}+3\sigma_\lambda}\int_{\bar{d}-3\sigma_d}^{\bar{d}+3\sigma_d}W(\theta,\bar{\theta},\Delta\theta)\Psi(\lambda,\bar{\lambda},\sigma_\lambda)\alpha(d,\lambda,n_p,\theta)F(d,\bar{d},\sigma_d)\mathrm{d}d\mathrm{d}\lambda\mathrm{d}\theta}{2\pi\int_{\theta_a}^{\pi}\int_{\bar{\lambda}-3\sigma_\lambda}^{\bar{\lambda}+3\sigma_\lambda}\int_{\bar{d}-3\sigma_d}^{\bar{d}+3\sigma_d}\sin(\theta)\Psi(\lambda,\bar{\lambda},\sigma_\lambda)\alpha(d,\lambda,n_p,\theta)F(d,\bar{d},\sigma_d)\mathrm{d}d\mathrm{d}\lambda\mathrm{d}\theta}. \quad \text{(A3)}$$

[61] The spectral response of the sensor, Ψ, is defined by a centroid wavelength $\bar{\lambda}$ and standard deviation σ_λ. The parameter α is the amplitude of unpolarized light scattering by the microspheres computed from Lorenz-Mie theory [*Bohren and Huffman*, 1983] and F is the microsphere size distribution defined by a centroid $\bar{d}$ and standard deviation σ_d. The σ_λ of the laser source was less than 1 nm, so, when convolved with the bandwidth of the detector interference filter, Ψ was a negligible parameter for the MASCOT and could be ignored. The outer integral in the denominator was applied from θ_a, the acceptance angle of the ac9 (0.93°), to π radians. Size distributions were assumed Gaussian and their scattering contribution numerically evaluated over ±3 standard deviations with $\mathrm{d}d < 0.06\sigma_d$. The normal dispersion refractive index equation for polystyrene measured by *Ma et al.* [2003] was used. The refractive index of the pure water medium was taken from *Quan and Fry* [1995].

[62] Angular weighting functions W for each scattering measurement were computed numerically with details provided by *Sullivan et al.* [2012] (Figure A2). They were also evaluated experimentally by translating a filament along the center of the source beam axis through the sample volume in air orthogonally to the plane of the detector array (Figure A2). Since the entire sample volume for each scattering measurement was not resolved in the experiment (only a plane through the middle of the source beam) and the filament exhibited edge effects, the measurements are only approximate. The results are nonetheless meaningful in helping to validate the shape ($\bar{\theta}$ and $\Delta\theta$) from the numerical results. Because of the caveats with the experimental evaluation of the weighting functions, the numerically computed W were used for all phase function calculations. Centroid angles $\bar{\theta}$, defined as the midpoint of each of the weighting functions (i.e., where $W(\theta)$ integrated from 0° to $\bar{\theta}$ was equivalent to $W(\theta)$ integrated from $\bar{\theta}$ to 180°), were no more than 0.4° different from the scattering angle defined by the intersection of the centers of the source and detector beams. Throughout the paper β is only referenced with respect to $\bar{\theta}$ rounded to the nearest unit angle, although the full $W(\theta)$ for each angle should be implicitly acknowledged.

[63] Source reference counts R exhibited electronic drift, usually correlated with measured dark offset drifts during casts. Because of this short-term drift, reference counts could not be applied on a measurement-by-measurement basis without injecting bias into the data and thus were only useful in evaluating long-term drift in laser power. There are several lines of evidence suggesting drift in actual laser power is very small over periods of years. First, reference count drift was usually correlated with dark offset count drift for the scattering detectors, indicating the drift was similarly electronic drift in the reference background counts. Second, power meter measurements of the source beam in the lab have shown excellent stability (<1% variation as per laser specifications) over time. Third, scaling factor values obtained from several calibrations over the course of several years with the same microsphere population have agreed within 2%. Fourth, averaged reference counts from all cruises show no long-term pattern, with a standard deviation around the mean of 4%, which is probably residual bias from short-term electronic drift as opposed to actual laser power drift. As a result, the R_{cal}/R_m term in equation (A1) was set at 1.

[64] For each scattering channel, the computed phase function value $\tilde{\beta}_p(\bar{\theta}_i)$ was divided by the experimentally derived M_i to obtain f_i. With D_i, f_i, and ε in hand, the instrument may be used in any unknown solution to provide $\beta(\bar{\theta}_i)$ using equation (A1), although caution should be exercised with respect to the ε value being specific for suspensions of particles in natural waters. From independent calibrations with NIST-traceable 0.2 and 2 μm beads, measurement accuracy is estimated between 2% and 4% for the 17 scattering channels.

[65] **Acknowledgments.** We acknowledge the assistance of Nick Hall-Patch at the Institute of Ocean Sciences with data collection. Howard Gordon, Emmanuel Boss, and Fraser Dalgleish provided valuable comments on the manuscript. This research was carried out as part of the Office of Naval Research RaDyO program (Radiance in a Dynamic Ocean) under contracts N00014-06-C-0027, N00014-06-1-0072, N00014-06-1-0379, and N00014-06-1-0069 and was also supported by Fisheries and Oceans Canada (S.V.), NASA contract NNX09AV55G (M.T.), ONR contract N00014-08-C-0658 (M.T.) and WET Labs.

References

Aas, E. (1981), The refractive index of phytoplankton, *Rep. 46*, 61 pp., Inst. of Geophys., Univ. of Oslo, Oslo.

Agrawal, Y. C., and O. Mikkelsen (2009), Empirical forward scattering phase functions from 0.08 to 16 deg for randomly shaped terrigenous 1–21 μm sediment grains, *Opt. Express*, *17*(11), 8805–8814, doi:10.1364/OE.17.008805.

Agrawal, Y. C., and H. C. Pottsmith (2000), Instruments for particle size and settling velocity observations in sediment transport, *Mar. Geol.*, *168*, 89–114, doi:10.1016/S0025-3227(00)00044-X.

Baldy, S. (1988), Bubbles in the close vicinity of breaking waves: Statistical characteristics of the generation and dispersion mechanism, *J. Geophys. Res.*, *93*(C7), 8239–8248, doi:10.1029/JC093iC07p08239.

Bi, L., P. Yang, G. W. Kattawar, and R. Kahn (2010), Modeling optical properties of mineral aerosol particles by using nonsymmetric hexahedra, *Appl. Opt.*, *49*, 334–342, doi:10.1364/AO.49.000334.

Bohren, C. F., and D. R. Huffman (1983), *Absorption and Scattering of Light by Small Particles*, 530 pp., John Wiley, New York.

Boss, E., M. S. Twardowski, and S. Herring (2001), Shape of the particulate beam attenuation spectrum and its inversion to obtain the shape of the particulate size distribution, *Appl. Opt.*, *40*, 4885–4893, doi:10.1364/AO.40.004885.

Boss, E., W. Slade, and P. Hill (2009), Effect of particulate aggregation in aquatic environments on the beam attenuation and its utility as a proxy for

particulate mass, *Opt. Express*, *17*(11), 9408–9420, doi:10.1364/OE.17.009408.

Brown, O. B., and H. R. Gordon (1973), Two component Mie scattering models of Sargasso Sea particles, *Appl. Opt.*, *12*, 2461–2465, doi:10.1364/AO.12.002461.

Buonassissi, C., and H. Dierssen (2010), A regional comparison of particle size distributions and the power law approximation in oceanic and estuarine surface waters, *J. Geophys. Res.*, *115*, C10028, doi:10.1029/2010JC006256.

Campbell, J. W. (1995), The lognormal distribution as a model for bio-optical variability in the sea, *J. Geophys. Res.*, *100*, 13,237–13,254, doi:10.1029/95JC00458.

Campbell, J. W., and C. M. Yentsch (1989), Variance within homogeneous phytoplankton populations, part II: Analysis of clonal cultures, *Cytometry*, *10*, 596–604, doi:10.1002/cyto.990100515.

Carder, K. L., P. R. Betzer, and D. W. Eggimann (1974), Physical, chemical, and optical measures of suspended particle concentrations: Their intercomparison and application to the West African Shelf, in *Suspended Solids in Water*, edited by R. J. Gibbs, pp. 173–193, Plenum, New York.

Cartmill, J. W., and M. Y. Su (1993), Bubbles size distribution under saltwater and freshwater breaking waves, *Dyn. Atmos. Oceans*, *20*, 25–31, doi:10.1016/0377-0265(93)90046-A.

Clavano, W. R., E. Boss, and L. Karp-Boss (2007), Inherent optical properties of non-spherical marine-like particles—From theory to observation, *Oceanogr. Mar. Biol.*, *45*, 1–38, doi:10.1201/9781420050943.ch1.

Czerski, H., M. Twardowski, X. Zhang, and S. Vagle (2011a), Resolving size distributions of bubbles with radii less than 30 μm with optical and acoustical methods, *J. Geophys. Res.*, *116*, C00H11, doi:10.1029/2011JC007177.

Czerski, H., S. Vagle, D. M. Farmer, and N. Hall-Patch (2011b), Improvements to the methods used to measure bubble attenuation using and underwater acoustical resonator, *J. Acoust. Soc. Am.*, *130*, 3421–3430, doi:10.1121/1.3569723.

Deane, G. B., and M. D. Stokes (1999), Air entrainment processes and bubble size distributions in the surf zone, *J. Phys. Oceanogr.*, *29*, 1393–1403, doi:10.1175/1520-0485(1999)029<1393:AEPABS>2.0.CO;2.

Deane, G. B., and M. D. Stokes (2002), Scale dependence of bubble creation mechanisms in breaking waves, *Nature*, *418*, 839–844, doi:10.1038/nature00967.

Egan, W. G. (1982), Optical properties of standard aerosols: A report of measurements for the First International Workshop, in *Light Absorption by Aerosol Particles*, edited by H. E. Gerber and E. E. Hindman, pp. 197–230, Spectrum, Hampton, Va.

Epstein, B. (1947), The mathematical description of certain breakage mechanisms leading to the logarithmico-normal distribution, *J. Franklin Inst.*, *244*, 471–477, doi:10.1016/0016-0032(47)90465-1.

Farmer, D. M., S. Vagle, and A. D. Booth (1998), A free-flooding acoustical resonator for the measurement of bubble size distributions, *J. Atmos. Oceanic Technol.*, *15*, 1132–1146, doi:10.1175/1520-0426(1998)015<1132:AFFARF>2.0.CO;2.

Gardner, W. D., I. D. Walsh, and M. J. Richardson (1993), Biophysical forcing of particle production and distribution during a spring bloom in the North Atlantic, *Deep Sea Res. Part II*, *40*, 171–195, doi:10.1016/0967-0645(93)90012-C.

Glazman, R. E. (1983), Effects of adsorbed films on gas bubble radial oscillations, *J. Acoust. Soc. Am.*, *74*(3), 980–986, doi:10.1121/1.389844.

Gordon, H. R. (2007), Rayleigh-Gans scattering approximation: Surprisingly useful for understanding backscattering from disk-like particles, *Opt. Express*, *15*(9), 5572–5588, doi:10.1364/OE.15.005572.

Gordon, H. R., and O. B. Brown (1972), A theoretical model of light scattering by Sargasso Sea particulates, *Limnol. Oceanogr.*, *17*, 826–832, doi:10.4319/lo.1972.17.6.0826.

Groundwater, H., M. Twardowski, H. Dierssen, A. Sciandre, and S. Freeman (2012), Determining oceanic particle size distributions and particle composition: A new SEM-EDS protocol with validation and comparison to other methods, *J. Atmos. Oceanic Technol.*, doi:10.1175/JTECH-D-11-00026.1, in press.

Jonasz, M. (1987), Nonsphericity of suspended marine particles and its influence on light scattering, *Limnol. Oceanogr.*, *32*, 1059–1065, doi:10.4319/lo.1987.32.5.1059.

Jonasz, M., and H. Prandke (1986), Comparison of measured and computed light scattering in the Baltic, *Tellus Ser. B*, *38*, 144–157, doi:10.1111/j.1600-0889.1986.tb00096.x.

Katz, J. (1978), Determination of solid nuclei and bubble distributions in water by holography, *Eng. Appl. Sci. Div. Rep. 183*, Calif. Inst. of Technol., Pasadena.

Kirk, J. T. O. (1992), Monte Carlo modeling of the performance of a reflective tube absorption meter, *Appl. Opt.*, *31*(30), 6463–6468, doi:10.1364/AO.31.006463.

Kitchen, J. (1977), Particle size distributions and the vertical distribution of suspended matter in the upwelling region off Oregon, MSc thesis, 118 pp., Oreg. State Univ., Corvallis.

Kopelevich, O. V. (1983), Small-parameter model of optical properties of sea water (in Russian), in *Ocean Optics*, vol. 1, *Physical Ocean Optics*, edited by A. S. Monin, pp. 208–234, Nauka, Moscow.

Kullenberg, G. (1974), Observed and computed scattering functions, in *Optical Aspects of Oceanography*, edited by N. G. Jerlov and E. Steeman-Nielsen, pp. 25–49, Academic, San Diego, Calif.

Lai, F. S., S. K. Friedlander, J. Pich, and G. M. Hidy (1972), The self-preserving particle size distribution for Brownian coagulation in the free-molecule regime, *J. Colloid Interface Sci.*, *39*, 395–405, doi:10.1016/0021-9797(72)90034-3.

Lambert, C. E., C. Jehanno, N. Silverberg, J. C. Brun-Cottan, and R. Chesselet (1981), Log-normal distribution of suspended particles in the open ocean, *J. Mar. Res.*, *39*, 77–98.

Lawson, C. L., and R. J. Hanson (1974), *Solving Least Squares Problems*, 340 pp., Prentice-Hall, Englewood Cliffs, N. J.

Longhurst, A. R., et al. (1992), Sub-micron particles in northwest Atlantic shelf water, *Deep Sea Res. Part A*, *39*, 1–7, doi:10.1016/0198-0149(92)90016-M.

Ma, X., J. Q. Lu, R. S. Brock, K. M. Jacobs, P. Yang, and X. Hu (2003), Determination of complex refractive index of polystyrene microspheres from 370 to 1610 nm, *Phys. Med. Biol.*, *48*, 4165–4172, doi:10.1088/0031-9155/48/24/013.

McKee, D., J. Piskozub, and I. Brown (2008), Scattering error corrections for in situ absorption and attenuation measurements, *Opt. Express*, *16*(24), 19,480–19,492, doi:10.1364/OE.16.019480.

Mishchenko, M. I., J. W. Hovenier, and L. D. Travis (2000), *Light Scattering by Nonspherical Particles*, 690 pp., Academic, New York.

Mobley, C. D., B. Gentili, H. R. Gordon, Z. Jin, G. W. Kattawar, A. Morel, P. Reinersman, K. Stamnes, and R. H. Stavn (1993), Comparison of numerical models for computing underwater light fields, *Appl. Opt.*, *32*, 7484–7504, doi:10.1364/AO.32.007484.

Pegau, W. S., D. Gray, and J. R. V. Zaneveld (1997), Absorption and attenuation of visible and near-infrared light in water: Dependence on temperature and salinity, *Appl. Opt.*, *36*, 6035–6046, doi:10.1364/AO.36.006035.

Peng, F., D. L. Johnson, and S. W. Effler (2002), Suspensoids in New York City's drinking water reservoirs: Turbidity apportionment, *J. Am. Water Resour. Assoc.*, *38*, 1453–1465, doi:10.1111/j.1752-1688.2002.tb04358.x.

Peng, F., S. W. Effler, D. O'Donnell, M. G. Perkins, and A. Weidemann (2007), Role of minerogenic particles in light scattering in lakes and a river in central New York, *Appl. Opt.*, *46*(26), 6577–6594, doi:10.1364/AO.46.006577.

Petzold, T. J. (1972), Volume scattering function for selected ocean waters, *Rep. SIO 72-78*, Scripps Inst. of Oceanogr., La Jolla, Calif.

Pfitsch, D. W., E. Malkiel, Y. Ronzhes, S. R. King, J. Sheng, and J. Katz (2005), Development of a free-drifting submersible digital holographic imaging system, *Oceans*, *1*, 690–696.

Pope, R. M., and E. S. Fry (1997), Absorption spectrum (380–700 nm) of pure water. Part II. Integrating cavity measurements, *Appl. Opt.*, *36*, 8710–8723, doi:10.1364/AO.36.008710.

Portugal, L. F., J. J. Judice, and L. N. Vicente (1994), A comparison of block pivoting and interior-point algorithms for linear least squares problems with nonnegative variables, *Math. Comput.*, *63*, 625–643, doi:10.1090/S0025-5718-1994-1250776-4.

Quan, X., and E. S. Fry (1995), Empirical equation for the index of refraction of seawater, *Appl. Opt.*, *34*, 3477–3480, doi:10.1364/AO.34.003477.

Ran, B., and J. Katz (1991), The response of microscopic bubbles to sudden changes in the ambient pressure, *J. Fluid Mech.*, *224*, 91–115, doi:10.1017/S0022112091001660.

Reynolds, R., D. Stramski, V. M. Wright, and S. B. Woźniak (2010), Measurements and characterization of particle size distributions in coastal waters, *J. Geophys. Res.*, *115*, C08024, doi:10.1029/2009JC005930.

Schoonmaker, J. S., R. R. Hammond, A. L. Heath, and J. S. Cleveland (1994), Numerical model for prediction of sublittoral optical visibility, *Proc. SPIE*, *2258*, 685–702, doi:10.1117/12.190116.

Slade, W., E. Boss, and C. Russo (2011), Effects of particle aggregation and disaggregation on their inherent optical properties, *Opt. Express*, *19*(9), 7945–7959, doi:10.1364/OE.19.007945.

Stramski, D., and D. A. Kiefer (1991), Light scattering by microorganisms in the open ocean, *Prog. Oceanogr.*, *28*, 343–383, doi:10.1016/0079-6611(91)90032-H.

Sullivan, J. M., and M. S. Twardowski (2009), Angular shape of the oceanic particulate volume scattering function in the backward direction, *Appl. Opt.*, *48*, 6811–6819, doi:10.1364/AO.48.006811.

Sullivan, J. M., M. S. Twardowski, P. L. Donaghay, and S. A. Freeman (2005), Use of optical scattering to discriminate particle types in coastal waters, *Appl. Opt.*, *44*, 1667–1680, doi:10.1364/AO.44.001667.

Sullivan, J. M., M. S. Twardowski, J. R. V. Zaneveld, and C. Moore (2012), Measuring optical backscattering in water, in *Light Scattering Reviews*, Praxis, Chichester, U. K., in press.

Talapatra, S., A. R. Nayak, C. Zhang, J. Hong, J. Katz, M. Twardowski, J. Sullivan, and P. Donaghay (2010), Characterization of organisms, particles, and bubbles in the water column using a free-drifting, submersible, digital holography system, paper presented at Ocean Optics XX, Oceanogr. Soc., Anchorage, Alaska, 27 Sep to 1 Oct.

Terrill, E. J., W. K. Melville, and D. Stramski (2001), Bubble entrainment by breaking waves and their influence on optical scattering in the upper ocean, *J. Geophys. Res.*, *106*(C8), 16,815–16,823, doi:10.1029/2000JC000496.

Twardowski, M. S., J. M. Sullivan, P. L. Donaghay, and J. R. V. Zaneveld (1999), Microscale quantification of the absorption by dissolved and particulate material in coastal waters with an ac-9, *J. Atmos. Oceanic Technol.*, *16*(6), 691–707, doi:10.1175/1520-0426(1999)016<0691:MQOTAB>2.0.CO;2.

Twardowski, M. S., E. Boss, J. B. Macdonald, W. S. Pegau, A. H. Barnard, and J. R. V. Zaneveld (2001), A model for estimating bulk refractive index from the optical backscattering ratio and the implications for understanding particle composition in case I and case II waters, *J. Geophys. Res.*, *106*, 14,129–14,142, doi:10.1029/2000JC000404.

Twardowski, M. S., M. Lewis, A. Barnard, and J. R. V. Zaneveld (2005), In-water instrumentation and platforms for ocean color remote sensing applications, in *Remote Sensing of Coastal Aquatic Waters*, edited by R. Miller, C. Del Castillo, and B. McKee, pp. 69–100, Springer, Dordrecht, Netherlands, doi:10.1007/978-1-4020-3100-7_4.

Twardowski, M. S., H. Claustre, S. A. Freeman, D. Stramski, and Y. Huot (2007), Optical backscattering properties of the "clearest" natural waters, *Biogeosciences*, *4*, 1041–1058, doi:10.5194/bg-4-1041-2007.

Twomey, S. (1977), *Introduction to the Mathematics of Inversion in Remote Sensing and Indirect Measurements*, vol. 243 pp., Elsevier Sci., Amsterdam.

Ulloa, O., S. Sathyendranath, and T. Platt (1994), Effect of the particle-size distribution on the backscattering ratio in seawater, *Appl. Opt.*, *33*, 7070–7077, doi:10.1364/AO.33.007070.

Vaillancourt, R. D., and W. M. Balch (2000), Size distribution of marine submicron particles determined by flow field-flow fractionation, *Limnol. Oceanogr.*, *45*, 485–492, doi:10.4319/lo.2000.45.2.0485.

van de Hulst, H. C. (1981), *Light Scattering by Small Particles*, 470 pp., Dover, New York.

Voss, K. J., W. M. Balch, and K. A. Kilpatrick (1998), Scattering and attenuation properties of Emiliania huxleyi cells and their detached coccoliths, *Limnol. Oceanogr.*, *43*, 870–876, doi:10.4319/lo.1998.43.5.0870.

Wells, M. L., and E. D. Goldberg (1992), Marine submicron particles, *Mar. Chem.*, *40*, 5–18, doi:10.1016/0304-4203(92)90045-C.

Yamasaki, A., H. Fukuda, R. Fukuda, T. Miyajima, T. Nagata, H. Ogawa, and I. Koike (1998), Submicrometer particles in northwest Pacific coastal environments: Abundance, size distribution, and biological origins, *Limnol. Oceanogr.*, *43*, 536–542, doi:10.4319/lo.1998.43.3.0536.

You, Y., G. Kattawar, K. J. Voss, P. Bhandari, J. Wei, M. Lewis, C. J. Zappa, and H. Schultz (2011a), Polarized light field under dynamic ocean surfaces: Numerical modeling compared with measurements, *J. Geophys. Res.*, *116*, C00H05, doi:10.1029/2011JC007278.

You, Y., A. Tonizzo, A. A. Gilerson, M. E. Cummings, P. Brady, J. M. Sullivan, M. S. Twardowski, H. M. Dierssen, S. A. Ahmed, and G. W. Kattawar (2011b), Measurements and simulations of polarization states of underwater light in clear oceanic waters, *Opt. Express*, *50*(24), 4873–4893.

Yount, D. E., E. W. Gillary, and D. C. Hoffman (1984), A microscopic investigation of bubble formation nuclei, *J. Acoust. Soc. Am.*, *76*, 1511–1521, doi:10.1121/1.391434.

Zaneveld, J. R. V., and H. Pak (1973), Method for the determination of the index of refraction of particles suspended in the ocean, *J. Opt. Soc. Am.*, *63*, 321–324, doi:10.1364/JOSA.63.000321.

Zaneveld, J. R. V., D. M. Roach, and H. Pak (1974), The determination of the index of refraction distribution of oceanic particulates, *J. Geophys. Res.*, *79*(27), 4091–4095, doi:10.1029/JC079i027p04091.

Zaneveld, J. R. V., J. C. Kitchen, and C. M. Moore (1994), The scattering error correction of reflecting-tube absorption meters, *Proc. SPIE*, *2258*, 44–55, doi:10.1117/12.190095.

Zhang, X., M. Lewis, M. Lee, B. Johnson, and G. Korotaev (2002), The volume scattering function of natural bubble populations, *Limnol. Oceanogr.*, *47*(5), 1273–1282, doi:10.4319/lo.2002.47.5.1273.

Zhang, X., L. Hu, and M.-X. He (2009), Scattering by pure seawater: Effect of salinity, *Opt. Express*, *17*, 5698–5710, doi:10.1364/OE.17.005698.

Zhang, X., M. Twardowski, and M. Lewis (2011), Retrieving compostion and sizes of oceanic particles subpopulations from the volume scattering function, *Appl. Opt.*, *50*(9), 1240–1259, doi:10.1364/AO.50.001240.

L. Bi, G. Kattawar, and Y. You, Department of Physics and Astronomy, Texas A&M University, College Station, TX 77843, USA.

H. Czerski, Graduate School of Oceanography, University of Rhode Island, Narragansett, RI 02882, USA.

S. Freeman, J. Sullivan, and M. Twardowski, Department of Research, WET Labs, 70 Dean Knauss Dr., Narragansett, RI 02882, USA. (mtwardo@wetlabs.com)

S. Vagle, Institute of Ocean Sciences, Fisheries and Oceans Canada, 9860 W. Saanich Rd., Sidney, BC V8L 4B2, Canada.

X. Zhang, Department of Earth System Science and Policy, University of North Dakota, Grand Forks, ND 58202, USA.